# 2-Phenylpyridine Appended Phenanthroline-Based Cyclometalated Ir(III) Photocatalysts for NADH oxidation and ROS Mediated Cancer Phototherapy

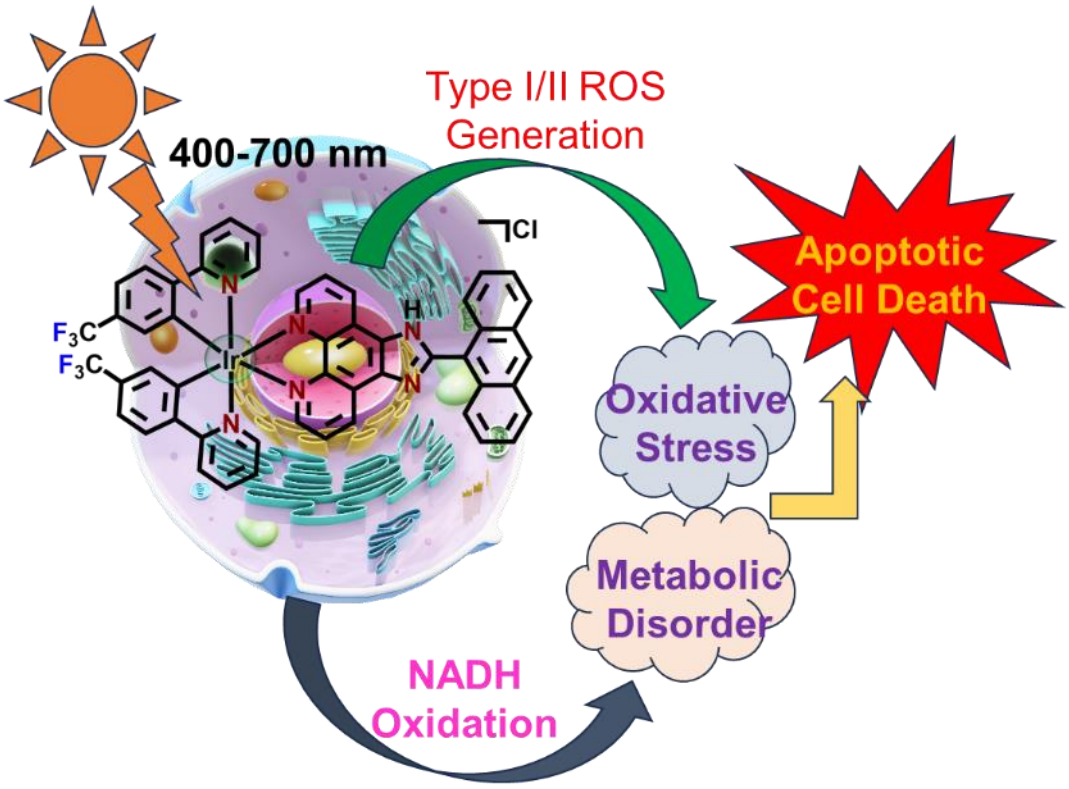


Published in *Chem. Asian J.* **2025**, e00681. DOI: https://doi.org/10.1002/asia.202500681.

## 2.1. Abstract

Three novel cyclometalated Ir(III) photocatalysts (**1**-**3**), *viz.* $[Ir(C^N)_2(ip)]Cl$ (**1**), $[Ir(C^N)_2(ph\text{-}ip)]Cl$ (**2**) and $[Ir(C^N)_2(aip)]Cl$ (**3**) (C^N= 2-(4-(Trifluromethyal)phenyl)pyridine; ip = 1H-imidazo[4,5-f][1,10]phenanthroline; ph-ip = 2-phenyl-1H-imidazo[4,5-f][1,10]phenanthroline; aip = 2-(anthracene-9-yl)-1H-imidazo[4,5-f][1,10]phenanthroline), were synthesized and thoroughly characterized. These photocatalysts exhibited absorption in the 350-480 nm range, making them suitable candidates for visible-light-mediated photocatalytic cancer therapy. Under visible-light (400-700 nm, 10 J $cm^{-2}$) exposure in a DMSO:PBS (1:99 v/v) solvent system, all three photocatalysts demonstrated high efficiency in facilitating NADH photo-oxidation, attaining turnover frequencies (TOFs) in the range of 499.14±26.51 to 697.44±26.37 $h^{-1}$, exceeding the performance of most of the previously reported Ir(III)-based photocatalysts. Mechanistic studies verified the involvement of type I and type II pathways for ROS generation. Cytotoxicity studies highlighted significant photocytotoxic effects of **1**-**3** in A549 cells, with **3** emerging as the most potent photocatalyst under light exposure. Additionally, the negligible dark and light cytotoxicity of **3** against HEK-293 cells demonstrated the safety profile of **3**. Furthermore, the mechanistic studies in A549 cells revealed that **3** promoted mitochondrial membrane depolarization and activated caspase-3/7-dependent apoptotic pathways through light-triggered ROS generation and NADH oxidation. These findings highlight **3** as a potent dual-action cancer phototherapeutic, capable of inducing synergistic type-I and type-II anticancer activity, and efficient NADH

photo-oxidation. This work presents a promising platform for developing multifunctional photocatalytic agents in cancer therapy.

**2.2. Introduction**

In **Chapter I**, several studies, including those from the groups of Sadler, Ruiz, Paira, and Huang, as well as our group, demonstrated that Ir(III) photocatalysts induce photocytotoxicity through a combination of NADH oxidation and ROS generation.[1-8] But, at the same time, despite these advances, these photocatalysts are found to show low TOF for photocatalytic NADH oxidation. For example, Sadler *et al*. reported a TOF of 100.4 $h^{-1}$ under blue light using an Ir(III)-based photocatalyst,[1] while Ruiz *et al*. achieved a TOF of 403.1 $h^{-1}$ under 465 nm light irradiation with another Ir(III)-based photocatalyst.[8] Herein, to address the challenge of achieving better performance for photocatalytic NADH oxidation, we have developed three novel polypyridyl-based cyclometalated Ir(III) photocatalysts (**1**-**3**), *viz.* $[Ir(C^N)_2(ip)]Cl$ (**1**), $[Ir(C^N)_2(ph\text{-}ip)]Cl$ (**2**) and $[Ir(C^N)_2(aip)]Cl$ (**3**) (C^N= 2-(4-(Trifluromethyal)phenyl)pyridine; ip = 1H-imidazo[4,5-f][1,10]phenanthroline; ph-ip = 2-phenyl-1H-imidazo[4,5-f][1,10]phenanthroline; aip = 2-(anthracene-9-yl)-1H-imidazo[4,5-f][1,10]phenanthroline) (Figure 2.1). The extended conjugation on the imidazole ring on the phenanthroline ligand was aimed at improving the photoinduced NADH oxidation activity.[9,10] The 1,10-phenanthroline derivatives were chosen due to their strong light-absorbing properties.[11-13] The extended π-conjugation in ph-ip and aip ligands was anticipated to decrease the HOMO-LUMO energy gap and enhance the photocatalysts' electron-accepting ability and reduction potential, thereby improving their photocatalytic efficacy.[7,9,14,15] Additionally, the -$CF_3$ group may further

enhance the electron-accepting ability and thereby the reduction potential of the photocatalysts.[16-18]

In this chapter, we present the synthesis, characterization, visible light-induced in-solution ROS generation, NADH oxidation, and visible light-triggered cytotoxic properties of **1**-**3**. Our findings confirmed that **1**-**3** not only exhibited better photocatalytic NADH oxidation activity under visible light (400-700 nm, 10 J $cm^{-2}$) but also generated ROS (*via* type I/II pathways), contributing to photocytotoxic effects against cancer cells. Their selective cytotoxicity toward cancer cells over normal cells, and the involvement of apoptotic pathways, have also been observed.

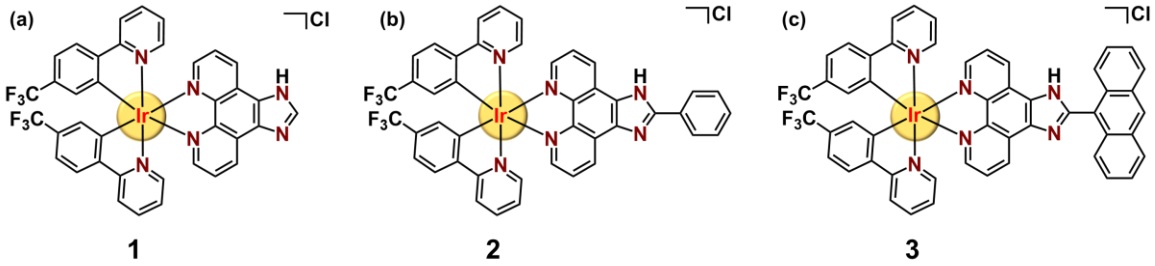


**Figure 2.1:** Structures of (a) **1**, (b) **2**, and (c) **3**.

## 2.3. Results and discussion

### 2.3.1. Synthesis and characterization

The photocatalysts, **1**-**3**, were synthesized using previously established synthetic methods with slight modifications.[5-7] Initially, the dimeric precursor, $[Ir(C^N)_2(Cl)]_2$, was heated at 50 °C for 24 h under an inert nitrogen atmosphere in a chloroform/methanol solvent system (2:1, v/v) containing a slight excess of the corresponding N^N ligand. Upon

completion of the reaction, the solution was cooled to ambient temperature, followed by filtration to eliminate any unreacted starting materials. Further, column chromatography on neutral alumina with methanol/n-hexane (1:99, v/v) mobile phase was employed to obtain the pure product. The purified **1-3** were obtained as deep yellow to reddish-brown solids with 54-68% yields. We performed various spectroscopic studies to confirm the structural integrity and purity of **1-3**, such as UV-Vis., fluorescence, elemental analysis, ESI-MS, HR-MS, and multinuclear NMR ($^{1}$H and $^{13}$C NMR). The ESI-MS analysis of **1** and **2** in MeOH exhibited molecular ion peaks at m/z = 857.1639 and 933.1930, respectively (Figures 2.2a, b). Whereas the HR-MS analysis of **3** in MeOH exhibited a molecular ion peak at m/z = 1033.2028, confirming the expected molecular compositions (Figure 2.2c).

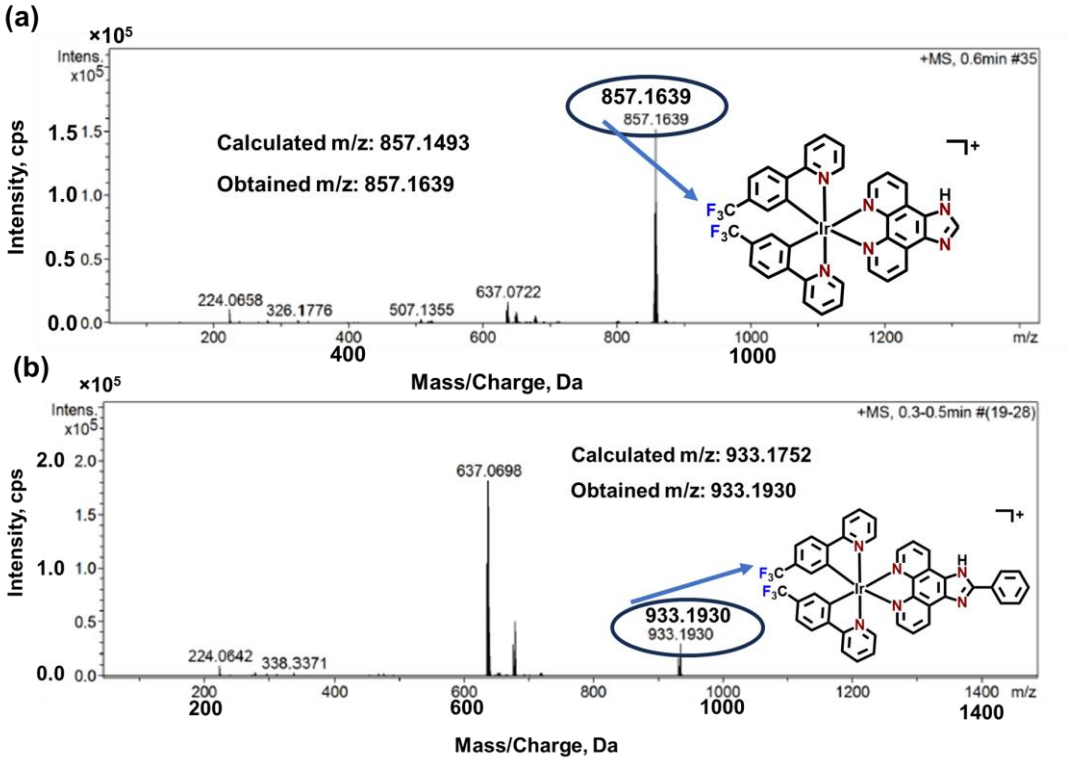


**Figure 2.2:** ESI-MS spectrum of (a) **1** and (b) **2** in methanol.

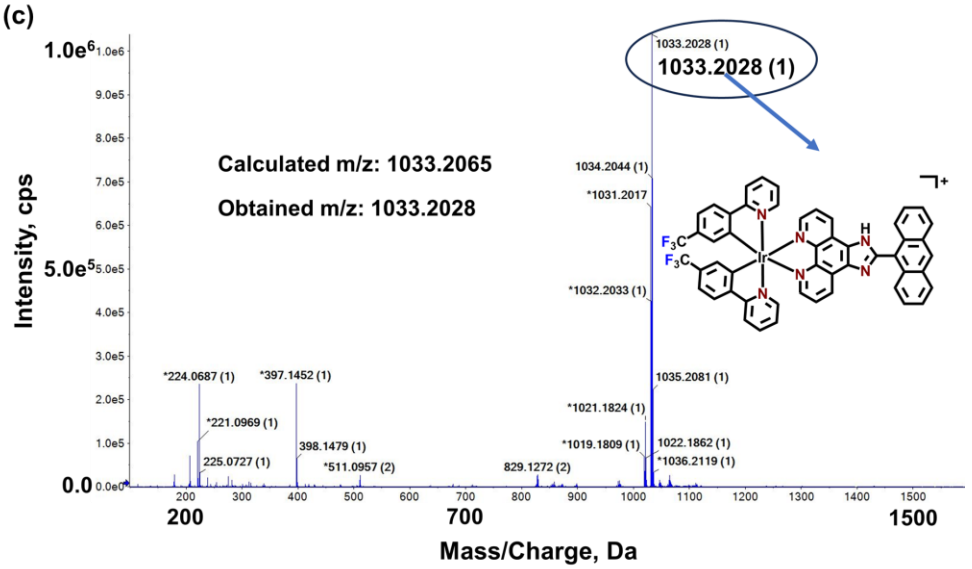


**Figure 2.2:** (c) HR-MS spectrum of **3** in methanol.

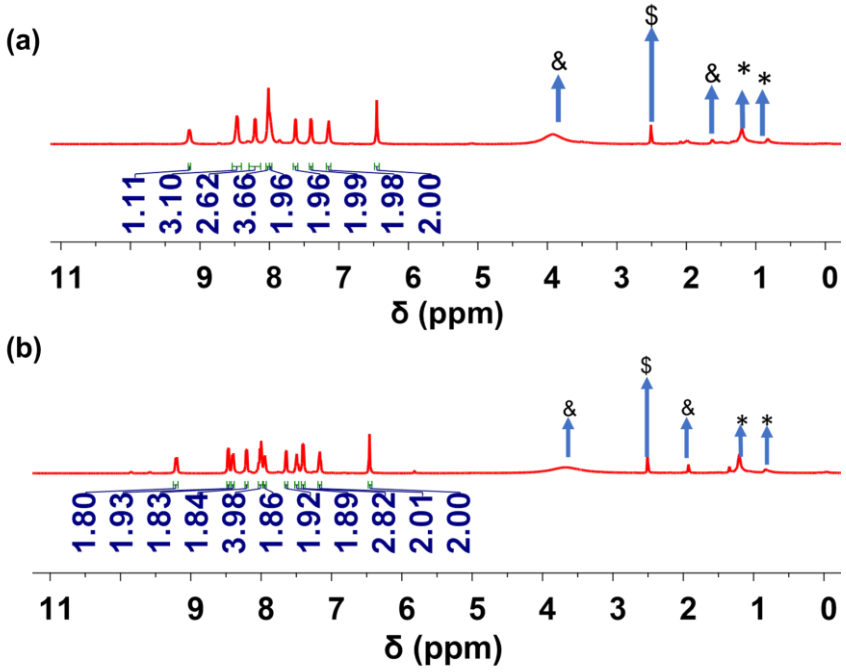


**Figure 2.3:** $^{1}$H NMR spectra of (a) **1**, and (b) **2** in DMSO-$d_6$ (500 MHz). (Residual solvent peaks: $^{\$}$DMSO-$d_6$, *n-hexane, and $^{\&}$diethyl ether.

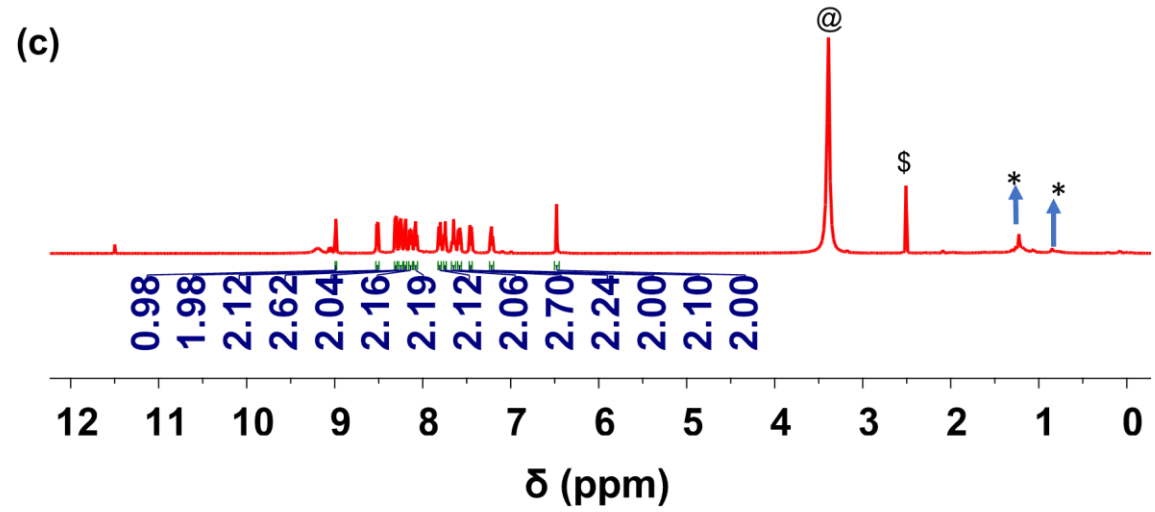


**Figure 2.3:** (c) $^{1}$H NMR spectra of **3** in DMSO-$d_6$ (500 MHz). (Residual solvent peaks: $^{@}H_2O$, $^{\$}$DMSO-$d_6$, *n-hexane.

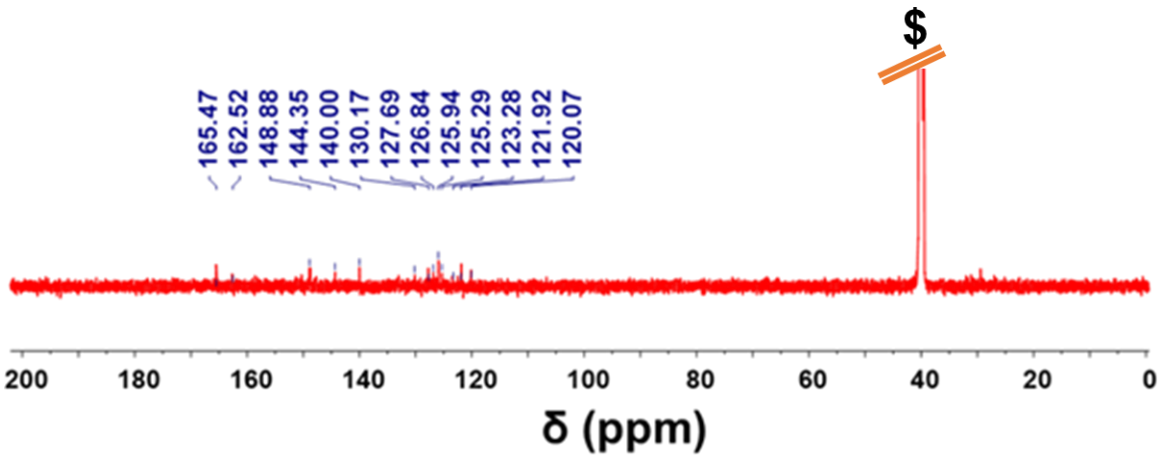


**Figure 2.4:** $^{13}$C NMR spectra of **1** in DMSO-$d_6$ (125 MHz). (Residual solvent peaks: $^{\$}$DMSO-$d_6$). The residual solvent peak was cutted for clarity.

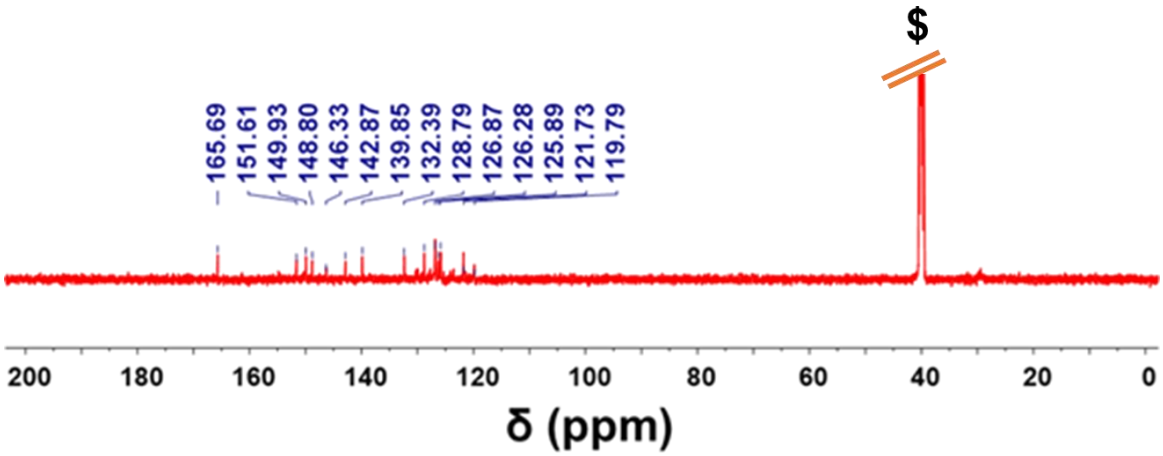


**Figure 2.5:** $^{13}$C NMR spectra of **2** in DMSO-$d_6$ (125 MHz). (Residual solvent peaks: $^{\$}$DMSO-$d_6$). The residual solvent peak was cutted for clarity.

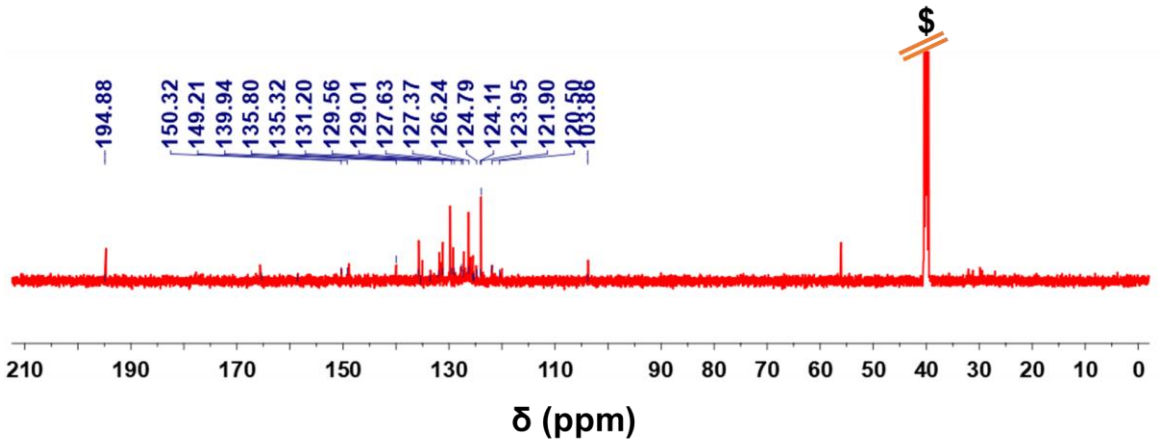


**Figure 2.6:** $^{13}$C NMR spectra of **3** in DMSO-$d_6$ (125 MHz). (Residual solvent peaks: $^{\$}$DMSO-$d_6$). The residual solvent peak was cutted for clarity.

The elemental analysis, $^{1}$H, and $^{13}$C NMR spectra **1-3** (in DMSO-$d_6$) (Figures 2.3a-c and 2.4, 2.5, and 2.6) reflected the purity of the photocatalyst. The $^{1}$H NMR spectra revealed well-resolved signals that supported the proposed structure. The peaks observed in the aromatic region (δ ~ 6.0–9.5 ppm) correspond to the aromatic protons of the 2-

phenylpyridine, ip, ph-ip, and aip ligands, consistent with the expected integration and chemical shifts (Figures 2.3a-c).[1,7,9] Characteristic signals for aromatic carbons were observed in the range of δ = 110-200 ppm (Figures 2.4, 2.5, and 2.6). The UV-Vis. studies of **1-3** were performed in DMSO:PBS solution (1:99, v/v) (Figure 2.7a). **1-3** displayed absorption features ≤ 370 nm, primarily arising from intra-ligand π→π* transitions.[9,19,20] Furthermore, a broad and less intense absorption was detected between 400-450 nm, which is indicative of metal-to-ligand charge transfer (MLCT).[9,19,20] These findings suggested that **1-3** possess efficient light absorption properties, which could be beneficial for phototherapeutic applications.[1-4] **1-3** in DMSO:PBS (1:99, v/v) solution exhibited an emission band between 450-550 nm upon excitation at 380 nm (Figure 2.7b).

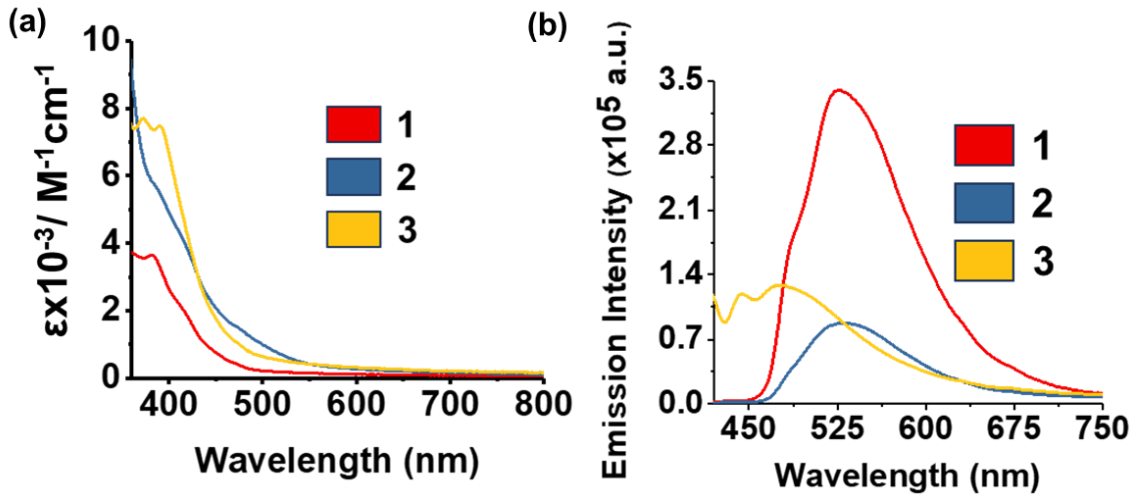


**Figure 2.7:** (a) Absorption spectra of **1-3** in DMSO:PBS (1:99 v/v) solution. (b) Emission spectra of **1-3** (50 μM each) in DMSO:PBS (1:99 v/v) [$\lambda_{ex}$ = 380 nm].

### 2.3.2. Solubility and Stability of 1-3

Photocatalysts **1-3** showed good solubility in methanol, ethanol, acetonitrile, DMF, and DMSO, while showing moderate solubility in $H_2O$. Further, the photostability study of **1-3** was performed at ambient temperature using the UV-Vis. absorption method (Figures 2.8a-c).[5-8] The absorption spectra of **1-3** in DMSO:PBS (1:99, v/v) solution did not show any notable change even after 7 h of light irradiation (400-700 nm, 10 J $cm^{-2}$), indicating the significant photostability of **1-3**. These findings suggested that these photocatalysts could serve as stable photocatalysts.

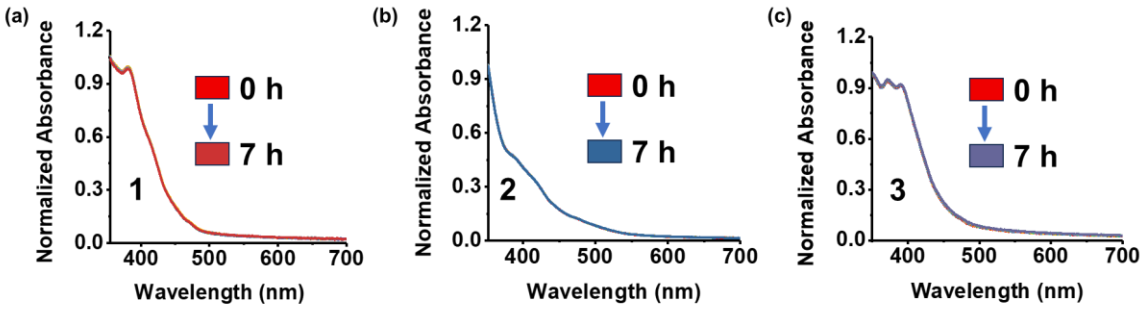


**Figure 2.8:** Photo-stability of (a) **1**, (b) **2**, (c) **3** (20 µM each) in DMSO:PBS (1:99, v/v) solution under visible light (400-700 nm, 10 J $cm^{-2}$) irradiation.

### 2.3.3. NADH photo-oxidation

The UV-Vis. absorption method was used to study the photocatalytic NADH oxidation property of **1-3**.[1-8] As shown in Figures 2.9a-c, the UV-Vis. spectra of NADH remained almost unchanged in the presence of the photocatalysts under the dark conditions. Moreover, no notable change in the NADH's UV-Vis. Spectra were observed after light irradiation in the absence of the photocatalysts (Figure 2.9d). However, when the solution

containing **1-3** (1 μM) and NADH (175 μM) was exposed to light irradiation for various intervals of time, the absorbance at λ = 339 nm corresponding to NADH decreased gradually (Figures 2.10a-c). This observation indicated that the photo-activated **1-3** catalyzed NADH oxidation and produced $NAD^+$. Extended π-conjugation on the imidazole-functionalized phenanthroline ligand in the photocatalysts significantly enhanced NADH photo-oxidation efficiency. **3** exhibited the highest catalytic activity among **1-3**, achieving a TOF of 697.4±26.4 $h^{-1}$, followed by **2** and **1**, which displayed TOF values of 609.2±25.6 $h^{-1}$ and 499.1±26.5 $h^{-1}$, respectively (Table 2.1). These TOF values are significantly higher than the previously reported Ir(III)- photocatalysts.[1,8,9] For example, Sadler *et al*., in their pioneering work on PCT, reported a TOF of 100.4 $h^{-1}$ under blue light irradiation (465 nm, 8.9 J $cm^{-2}$).[1] Recently, Paira *et al*. achieved a TOF of 1.5 $h^{-1}$.[9] Another study by Ruiz *et al*. demonstrated a TOF in the 240.0 $h^{-1}$ to 403.1 $h^{-1}$ range.[8] Importantly, the TOF achieved for **3** (697.4±26.4 $h^{-1}$) is *ca*. 160 times higher than the Ir(III) photocatalyst by Paira's group and almost 11 times higher than the pioneering work of the Sadler group, indicating the high efficiency of **3** as a photocatalyst for NADH oxidation. As we discussed in **section 1.7.2** of **Chapter I**, hydrogen peroxide ($H_2O_2$) is a by-product of NADH photo-oxidation; thus, we attempted to detect $H_2O_2$ during the catalytic process. The white color of the $H_2O_2$ detection strip showed no significant presence of $H_2O_2$ in the dark (Figure 2.10d). However, under light exposure, the color of the $H_2O_2$ strip changed to deep blue, indicating the generation of $H_2O_2$ and confirming the type I ROS generation mechanism. Overall, the above findings represent the potential of **1-3** as efficient photocatalysts for NADH photooxidation.

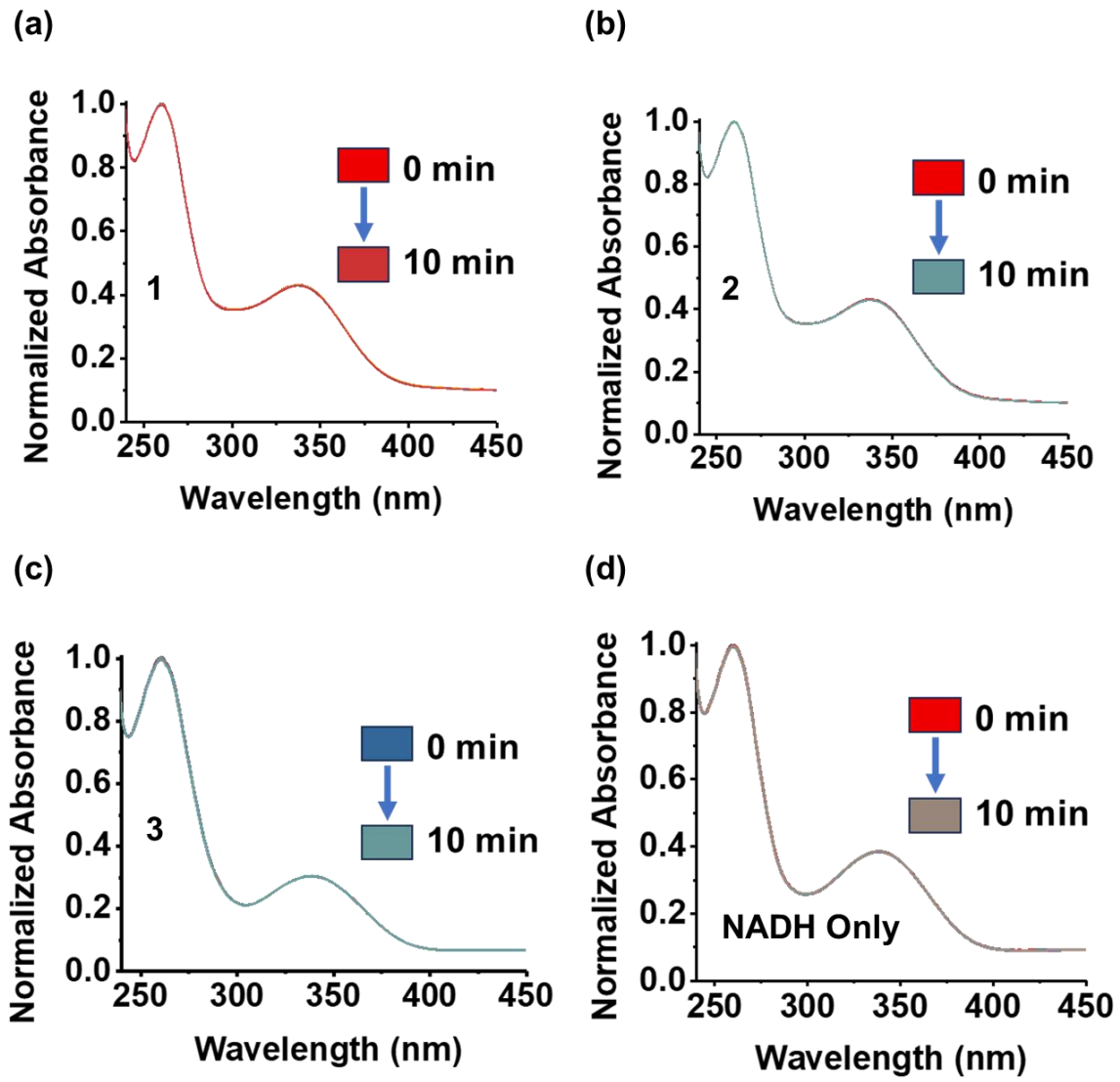


**Figure 2.9:** Absorption spectra of NADH (175 µM) in the presence of (a) **1**, (b) **2**, (c) **3** (1 µM each) in DMSO: PBS (1:99, v/v) in the dark. (d) No significant change in absorption spectra of NADH (175 µM) in DMSO:PBS (1:99, v/v) under visible light (400-700 nm, 10 J $cm^{-2}$) irradiation, representing the necessity of photocatalysts for photo-oxidation of NADH.

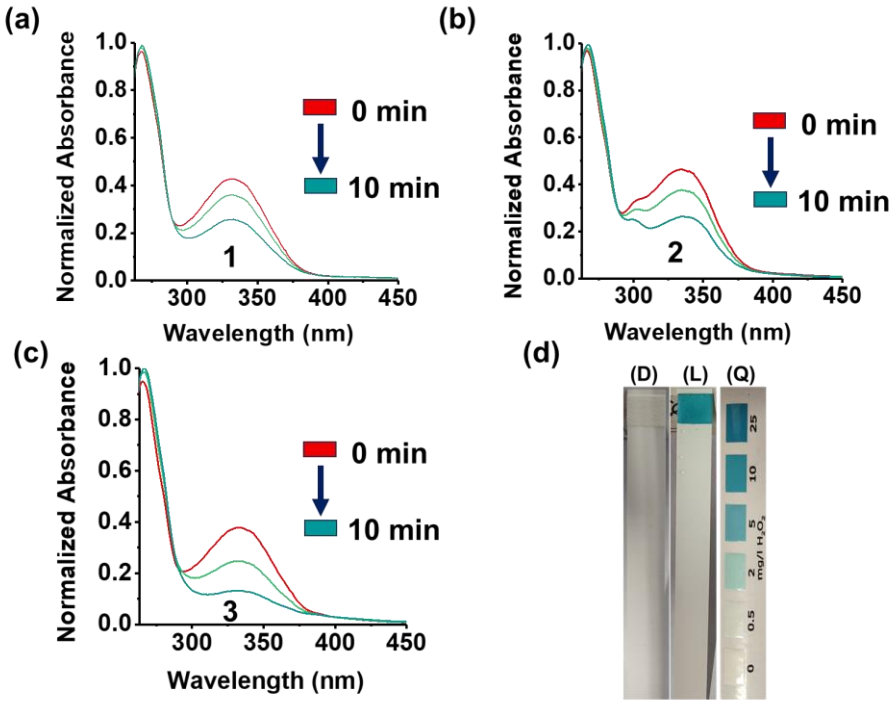


**Figure 2.10:** UV-Vis. absorption studies monitoring the light-induced NADH (175 μM) oxidation by (a) **1**, (b) **2**, and (c) **3** (1 μM each) in DMSO:PBS (1:99, v/v) solution under 400-700 nm light irradiation (10 J $cm^{-2}$). The experiment was repeated three times. The outcome of the results was expressed as mean ± SD. (d) Detection of $H_2O_2$ generation by **3** (1 μM) in the presence of NADH (175 μM) under light exposure (400-700 nm, 10 J $cm^{-2}$) using an $H_2O_2$ detection strip. D: dark, L: light, Q: $H_2O_2$ quantification scale.

**Table 2.1:** The TON and TOF of **1-3** and other Ir(III) based photocatalysts.

| **Photocatalysts** | **TON** | **TOF ($h^{-1}$)** |
|---|---|---|
| **1**[a] | 101.5±4.3 | 609.2±25.6 |
| **2**[a] | 83.2±4.4 | 499.1±26.5 |

| | | |
|---|---|---|
| **3**[a] | 116.2±4.4 | 697.4±26.4 |
| **Ir1**[b] | 50.2 | 100.4 |
| **[L1Ir]**[c] | - | 1.5 |
| **Ir4**[d] | 66.6 | 307.3 |
| **Ir5**[d] | 73.5 | 339.3 |
| **Ir6**[d] | 52.4 | 241.9 |
| **Ir7**[d] | 47.0 | 403.1 |

L1 = 2-(naphthalen-1-yl)-1H-imidazo[4,5-f][1,10]phenanthroline. [a]In DMSO:PBS (1:99, v/v) solution, light source: 400-700 nm, 10 J $cm^{-2}$. [b]In DMSO:PBS (0.5:99.5, v/v), dose: 8.9 J $cm^{-2}$ (taken from ref. 1). [c]Under 10 J $cm^{-2}$ light irradiation in PBS, light (400-700 nm) (taken from ref. 9). [d]Under 4.2 mW $cm^{-2}$ light exposure in DMF:PBS (5:95, v/v) (taken from ref. 8).

### 2.3.4. Singlet oxygen generation

ROS plays a crucial role in anticancer activity by inducing oxidative stress in cancer cells.[21,22] As many of the NADH oxidation photocatalysts have been reported to generate $^1O_2$ *via* type II mechanism,[1-8] we employed diphenylisobenzofuran (DPBF) as a probe for detecting the $^1O_2$ production possibility by **1-3**.[23,24] DPBF is a well-established probe that selectively reacts with $^1O_2$ and transforms into DPBF-$O_2$, decreasing its characteristic absorbance, thus providing a quantitative measure of $^1O_2$ production.[25-27] The study

revealed that upon treatment of **1**/**2**/**3**+Light, the absorbance of DPBF decreases significantly (Figures 2.11a-c), indicating the ability of **1-3** to generate $^1O_2$.

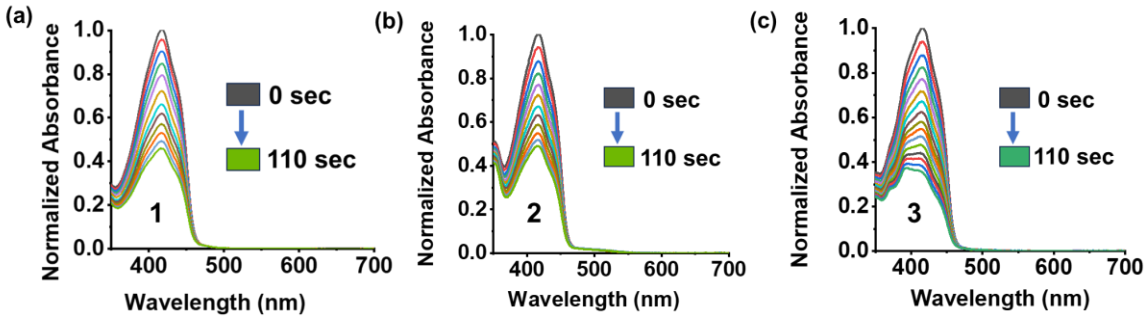


**Figure 2.11:** Time-dependent absorbance changes of DPBF (50 μM) indicating $^1O_2$ generation in the presence of (a) **1**, (b) **2**, and (c) **3** (1 μM each) upon light irradiation (400-700 nm, 10 J $cm^{-2}$). Solvent: DMSO:PBS (1:99, v/v).

We conducted control experiments to confirm the necessity of both light and the **1-3** for ROS generation (Figures 2.12a-d). When a DPBF solution was irradiated in the absence of **1-3**, the absorbance remained almost unchanged (Figure 2.12a), verifying that $^1O_2$ production resulted from **1-3**. Similarly, when **1-3** were mixed with DPBF but kept in the dark, no significant absorbance change was observed (Figures 2.12b-d), confirming the requirement for light activation in ROS generation. Further, to quantitatively assess $^1O_2$ production, the $^1O_2$ quantum yields ($\Phi_\Delta$) of **1-3** were measured using $[Ru(bpy)_3]Cl_2$ as a reference ($\Phi_\Delta$ = 0.22 in aqueous DMSO) (Figure 2.13). The calculated $\Phi_\Delta$ values were 0.14 for **1**, 0.16 for **2**, and 0.18 for **3**, reflecting a moderate efficiency of $^1O_2$ generation across the series.

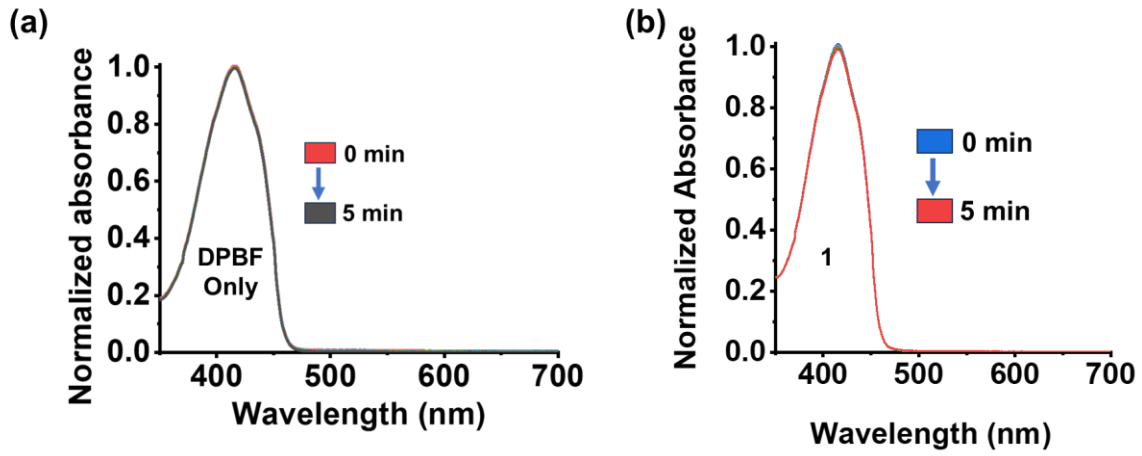


**Figure 2.12:** (a) No significant change in absorption spectra of DPBF (50 µM) only in DMSO:PBS (1:99, v/v) solution under visible light irradiation (Light source: 400-700 nm, 10 J $cm^{-2}$). The experiment was repeated three times independently with similar results. (b) Absorption spectra of DPBF (50 µM) in the presence of **1** (1 µM) in DMSO:PBS (1:99, v/v) under dark conditions.

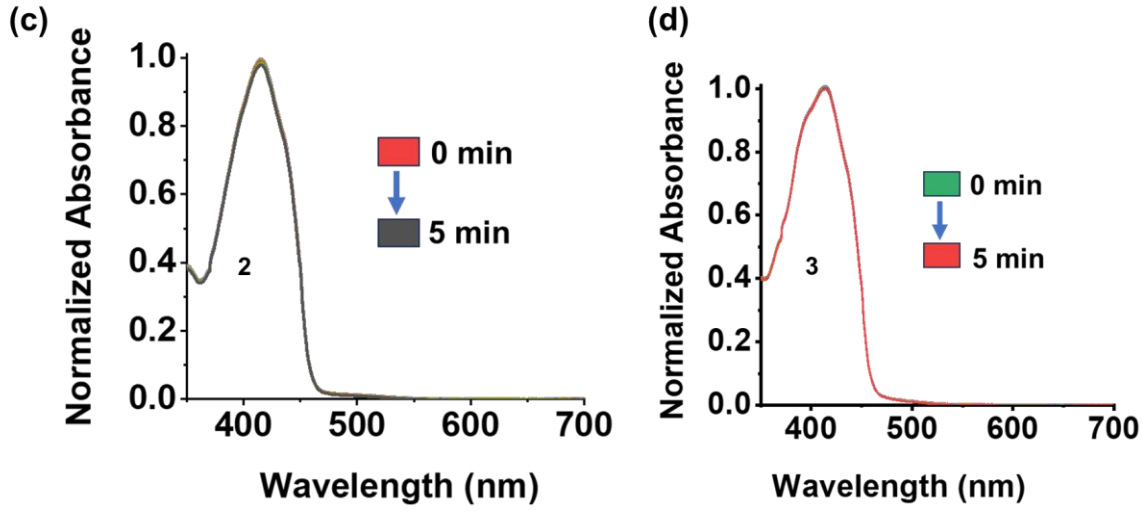


**Figure 2.12:** Absorption spectra of DPBF (50 µM) in the presence of (c) **2**, and (d) **3** (1 µM each) in DMSO:PBS (1:99, v/v) under dark conditions.

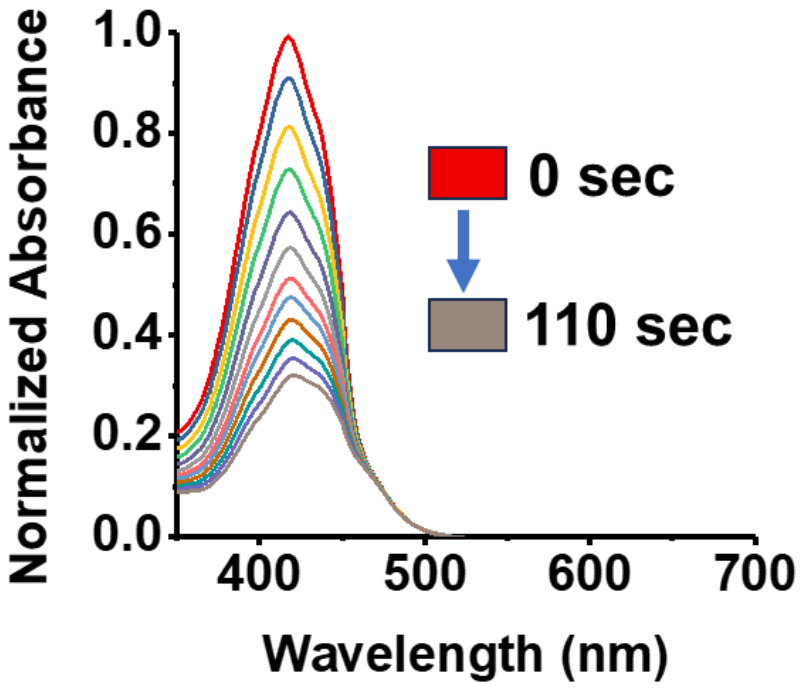


**Figure 2.13:** Time-dependent absorbance changes of DPBF (50 μM) indicating $^1O_2$ generation in the presence of $[Ru(bpy)_3]Cl_2$ (1 μM) upon light irradiation (400-700 nm, 10 J $cm^{-2}$). Solvent: DMSO:PBS (1:99, v/v).

### 2.3.5. Photocytotoxicity

Photocatalysts **1-3** exhibited in-solution ROS generation tendency. These generated ROS could produce oxidative stress inside the cancerous cell, which is often responsible for killing tumor cells.[28,29] Therefore, we study the cytotoxic activities of **1-3** under dark and light conditions. Cytotoxicity was evaluated using the MTT assay against A549 lung cancer cells and HEK-293 normal cells.[30,31] Cancer cells often exhibit altered metabolic activity, higher oxidative stress, and differential uptake of metal complexes compared to normal cells, which can influence the cytotoxic response.[32,33] Therefore, evaluating the cytotoxicity of **1-3** against both normal and cancerous cell lines is crucial for determining

their therapeutic potential and selectivity. The study revealed that **1**-**3** demonstrated significant photo-cytotoxicity against A549 cancer cell lines (Figure 2.14a), with $IC_{50}$ values ranging from 0.8±0.1 to 2.2±0.4 μM under light irradiation (Table 2.2). Among these, **3** exhibited the highest photocytotoxicity, with an $IC_{50}$ of 0.8±0.1 μM against A549 cancer cells. However, **1** and **2** displayed a bit lower photocytotoxic effects, with $IC_{50}$ values of 2.2±0.4 μM and 1.8±0.2 μM against A549 cancer cell lines, respectively (Table 2.2). **3** exhibited markedly enhanced photocytotoxicity compared to its analogs, displaying approximately three-fold greater activity than **1** and nearly two-fold higher efficacy than **2** under visible light irradiation. Additionally, **3** also exhibited higher photocytotoxicity than previously reported photocatalysts **1** and **2** against A549 cells.[1,29] This enhanced activity aligns with the trend observed in NADH oxidation TOF and $^1O_2$ generation, underscoring the critical role of increased π-conjugation in promoting photoreactivity and biological efficacy. **1**-**3** demonstrated low dark toxicity, with $IC_{50}$ values > 25.0 μM, indicating good safety profiles in the absence of light activation (Figure 2.14b). **3**, in particular, stood out the best with a phototoxicity index (PI = Dark $IC_{50}$/Light $IC_{50}$) > 30.9 μM (Table 2.2). Importantly, **3** also exhibited selectivity toward cancer cells, showing less toxicity against non-cancerous HEK-293 cells ($IC_{50}$ = 23.4 ± 2.0 μM) under light irradiation with a selectivity index (SI = Light $IC_{50}$ in normal cells/Light $IC_{50}$ in cancer cells) of 28.9 (Figure 2.15, Table 2.2). The superior performance of **3** over **1** and **2** is likely driven by its extended conjugation, efficient ROS generation, and NADH oxidation, contributing to its potent photocytotoxic activity. Collectively, these findings position **3** as a good candidate for further biological studies.

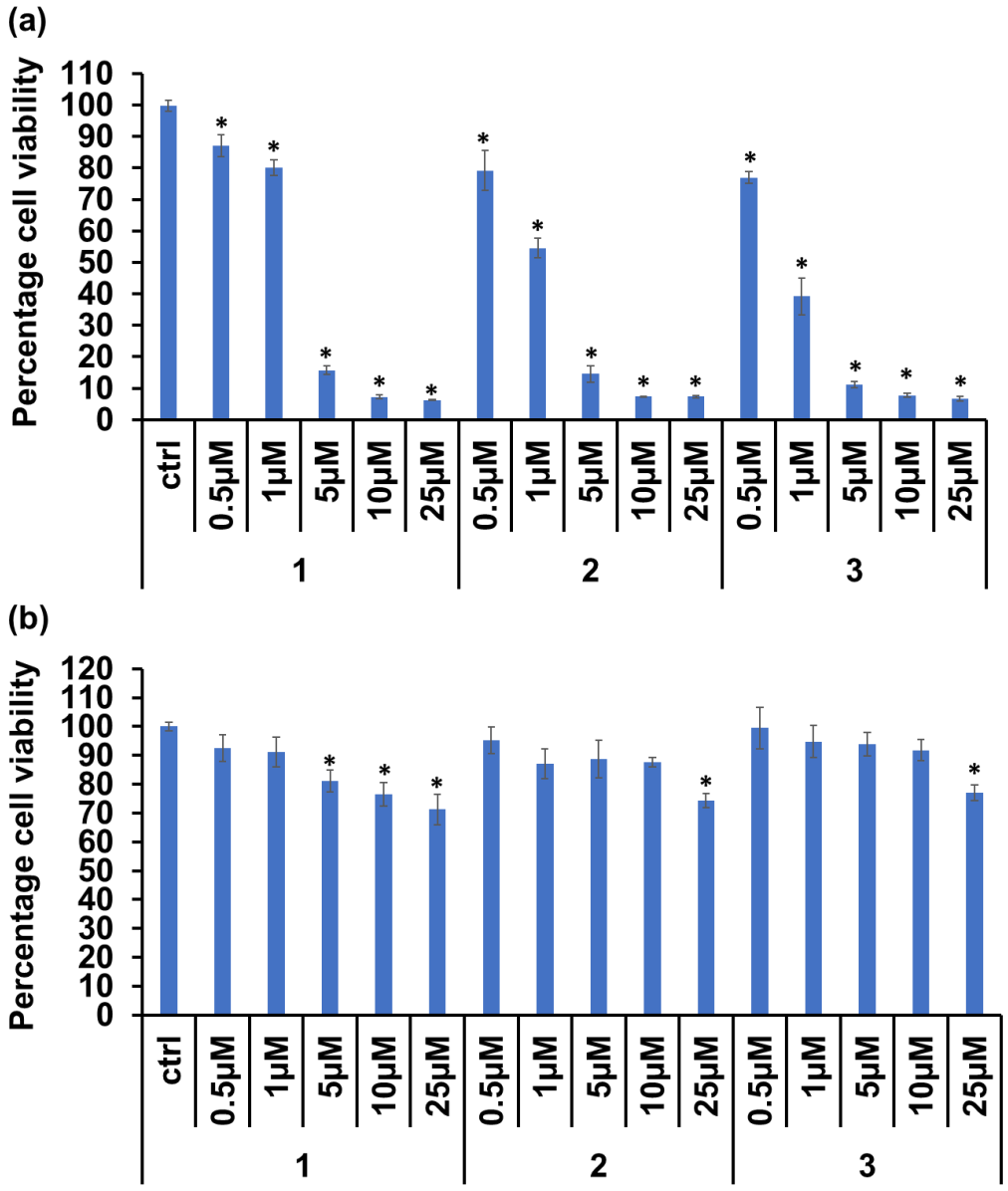


**Figure 2.14:** Cell viability plots of **1-3** against A549 cells on (a) light exposure (400-700 nm, 10 J $cm^{-2}$) or (b) under dark treatment. The outcome of the results was expressed as mean ± SD (error bars are standard deviations) of the three independent repeated experiments. The statistical analysis was done by One-way ANOVA followed by Tukey's Post Hoc Test (n=3). Where * denotes statistically significant ($p<0.05$).

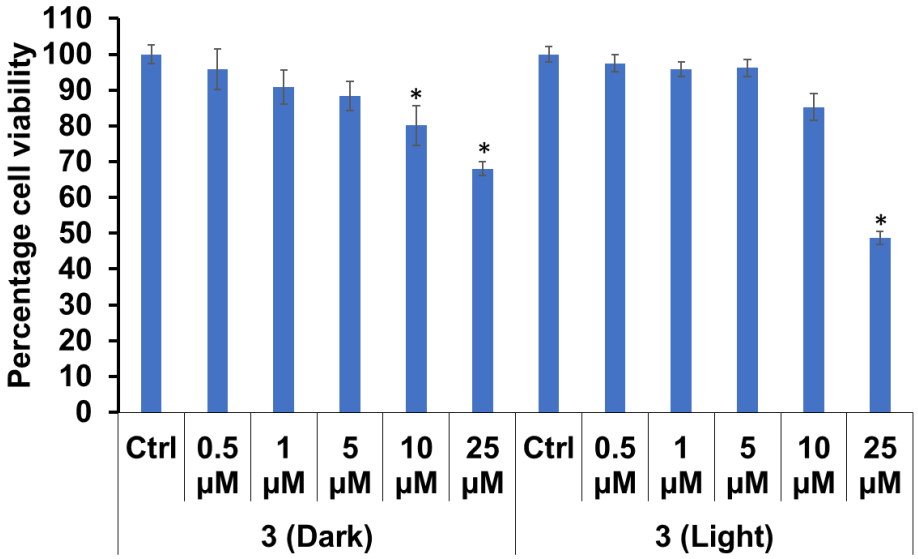


**Figure 2.15:** Cell viability plots of the MTT assay in normal **3**-treated HEK-293 cells on light exposure (400-700 nm, 10 J $cm^{-2}$). The outcome of the results was expressed as mean ± SD (error bars are standard deviations) of the three independent repeated experiments. The statistical analysis was done by One-way ANOVA followed by Tukey's Post Hoc Test (n=3). Where * denotes statistically significant ($p<0.05$).

**Table 2.2:** $IC_{50}$ (μM) values of **1-3** against cancerous and normal cell lines and some selected Ir(III)-based photocatalysts. (PI (phototoxicity index) = Dark $IC_{50}$/Light $IC_{50}$, and SI (selectivity index) = Light $IC_{50}$ in normal cells/Light $IC_{50}$ in cancer cells).

| **Photocatalyst** | **A549** | | | | **HEK-293** | |
|---|---|---|---|---|---|---|
| | Dark | Light | PI | SI | Dark | Light |
| **1**[a] | > 25.0 | 2.2±0.5 | >11.3 | | | |

| | | | | | | |
|---|---|---|---|---|---|---|
| **2**[a] | > 25.0 | 1.8±0.2 | >13.8 | | | |
| **3**[a] | > 25.0 | 0.8±0.1 | >30.9 | 28.9 | > 25.0 | 23.4±2.0 |
| **Ir1**[b] | 43.6±2.5 | 1.6±0.1 | 27.2 | | | |
| **Ir2**[c] | 62.3±2.6 | 1.1±0.3 | | | | |

[a]Cells were incubated with **1-3** for 6 h, followed by light exposure (400–700 nm, 10 J $cm^{-2}$) over 2 minutes. Recovery after irradiation: 18 h. For the dark group, the light irradiation step was absent. [b]Cells were incubated with **Ir1** for 2 h, followed by light exposure (465 nm, 8.9 J $cm^{-2}$) over 30 min. Recovery after irradiation: 46 h. For the dark group, the light irradiation step was absent (adapted from reference 1). [c]Cells were incubated with **Ir2** for 2 h, followed by light exposure (465 nm, 5.76 J $cm^{-2}$) over 20 min. Recovery after irradiation: 46 h. For the dark group, the light irradiation step was absent (adopted from reference 29). The outcome of the results was expressed as mean ± SD (error bars are standard deviations) of the three independent repeated experiments. The statistical analysis was done by One-way ANOVA followed by Tukey's Post Hoc Test (n=3). Where * denotes statistically significant ($p<0.05$)

### 2.3.6. In-cell ROS generation

2′,7′-Dichlorodihydrofluorescein diacetate (DCFH-DA) is widely used to detect intracellular ROS.[34,35] Once inside cells, it is deacetylated by esterases to form DCFH, which is then oxidized by ROS to generate the green fluorescent compound DCF, detectable by fluorescence microscopy.[36,37] In-solution ROS generation study with **1-3** exhibited their $^1O_2$ generation tendency. Inspired by this result, we used the DCFH-DA

method to explore the intracellular ROS generation tendency of the most potent photocatalyst, **3**, in A549 cancerous cells (Figure 2.16). The study revealed that the dark treatment of **3** (at its light $IC_{50}$ concentration) with A549 cells showed no significant enhancement in DCF green fluorescence compared to the control. This indicated negligible ROS generation in the absence of light. However, a substantial increase in green fluorescence intensity was detected upon **3** (at its light $IC_{50}$ concentration)+Light treatment, suggesting that **3** effectively generates ROS under light exposure. This study also confirmed the role of light activation in triggering ROS production, which could be essential for its potential therapeutic applications.

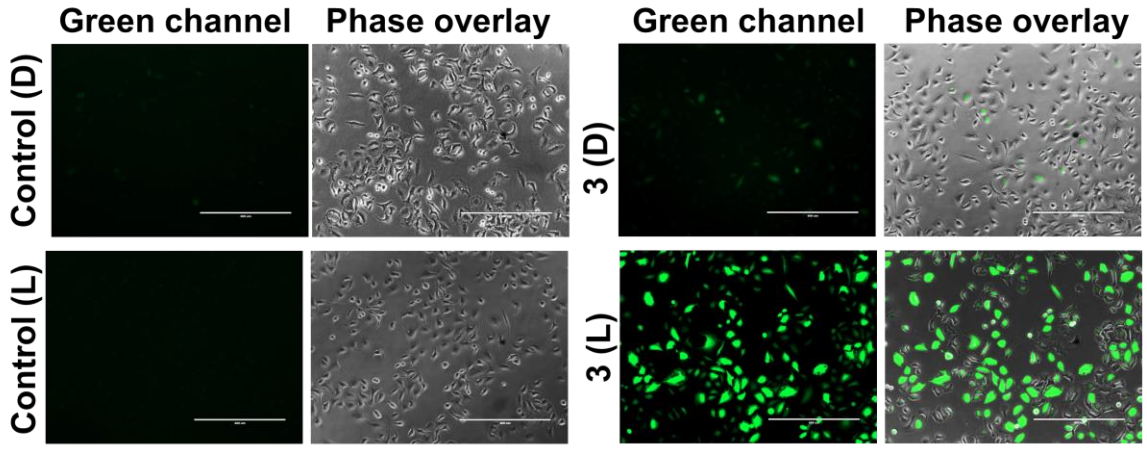


**Figure 2.16:** Intracellular ROS production by **3** (at light $IC_{50}$ concentration) in A549 cells under dark and 10 J $cm^{-2}$ light conditions (400–700 nm) was assessed using the DCFH-DA fluorescence probe (L = light; D = dark). Scale bar = 400 μm. Incubation time with **3:** 6 h, Light irradiation (400-700 nm, 10 J $cm^{-2}$) for 2 min. Recovery after irradiation: 18 h. For the dark group, the light irradiation step was absent. Scale bar: 400 μm. The experiment was repeated three times independently with similar results.

### 2.3.7. Mitochondrial depolarization

ROS production upon light exposure can induce oxidative damage to various cellular structures, including the mitochondrial membrane.[38,39] Such oxidative stress often results in the collapse of the mitochondrial membrane potential ($\Delta\Psi_m$), a vital marker of mitochondrial integrity and functionality.[38,39] The loss of $\Delta\Psi_m$, known as mitochondrial depolarization, is a key event in the apoptotic process and is frequently linked to impaired cellular function

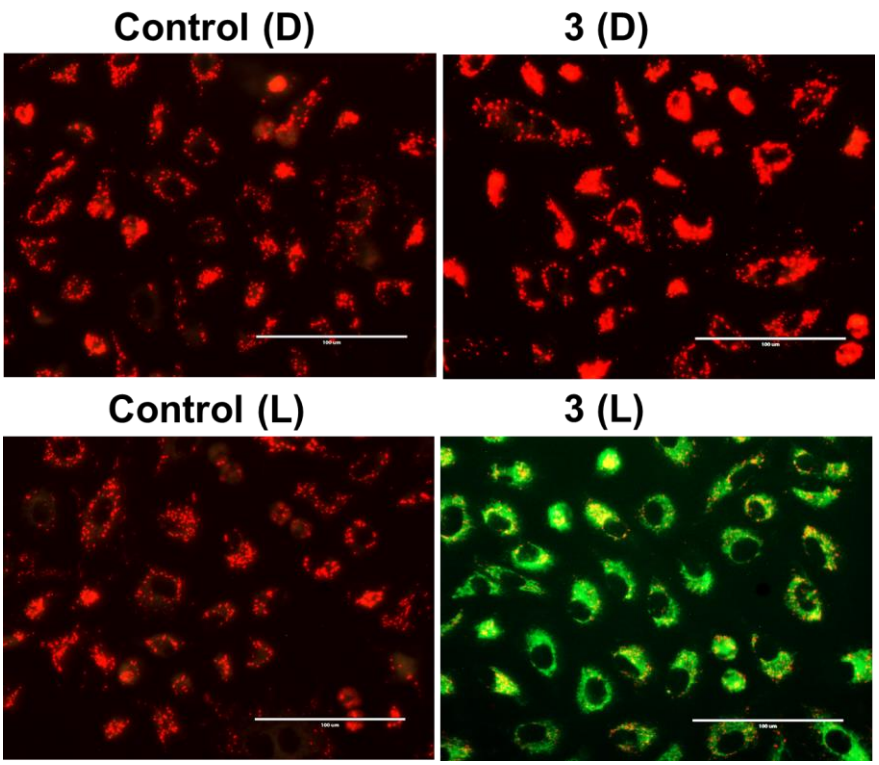


**Figure 2.17:** MMP changes in A549 cells treated with **3** (at its light $IC_{50}$ concentration), assessed using the JC-1 assay under dark and light conditions (L = light; D = dark). Incubation time with **3:** 6 h, Light irradiation (400-700 nm, 10 J $cm^{-2}$) for 2 min. Recovery after irradiation: 18 h. For the dark group, the light irradiation step was absent. Scale bar: 100 µm. The experiment was repeated three times independently with similar results.

and the initiation of programmed cell death.[40,41] To evaluate changes in mitochondrial membrane potential, the JC-1 assay was employed.[42,43] JC-1 is a membrane-permeant, cationic dye that selectively accumulates in mitochondria in a manner dependent on membrane potential.[42,43] This dye concentrates in normally functioning mitochondria and forms red aggregates, whereas in leaky mitochondria with compromised membranes, it is released into the cytosol and remains in a green monomeric state.[42,43] The study demonstrated that when A549 cells were exposed to **3** (at its light $IC_{50}$ concentration) under dark conditions, JC-1 exhibited red fluorescence (Figure 2.17). This confirmed that JC-1 remained in its aggregate form, and hence the preservation of $\Delta\Psi m$. However, upon treatment with light, the cells exhibited a prominent green fluorescence (Figure 2.17), indicating the monomeric form. This shift from J-aggregate to monomeric form, as well as red to green fluorescence, confirmed mitochondrial depolarization, demonstrating that light-activated **3** disrupts mitochondrial integrity, likely contributing to its cytotoxic effects.

### 2.3.8. Cell death mechanism

The observed ROS generation and mitochondrial membrane potential (MMP) disruption upon treatment with **3** (at its light $IC_{50}$ concentration)+Light prompted us to investigate the mechanism of cell death. To determine whether the induced cytotoxicity follows an apoptotic pathway, we performed Hoechst/PI dual staining, which differentiates between live, apoptotic, and necrotic cells based on nuclear morphology and membrane integrity.[44,45] Hoechst permeates all cells and binds to DNA, emitting blue fluorescence, whereas propidium iodide (PI) selectively enters cells with compromised membranes, emitting red fluorescence.[46] Apoptotic cells exhibit chromatin condensation and nuclear

fragmentation, whereas necrotic cells display diffuse red fluorescence due to membrane rupture. As shown in Figure 2.18a, A549 cells treated with **3** at its light $IC_{50}$ concentration under light conditions exhibited strong red fluorescence from PI and blue fluorescence from Hoechst. The overlay images displayed pink emission, indicative of an apoptotic cell death.[44,45,47] In contrast, cells treated with **3** (at its light $IC_{50}$ concentration) in the dark showed only weak red fluorescence (Figure 2.18a), suggesting low toxicity without light,

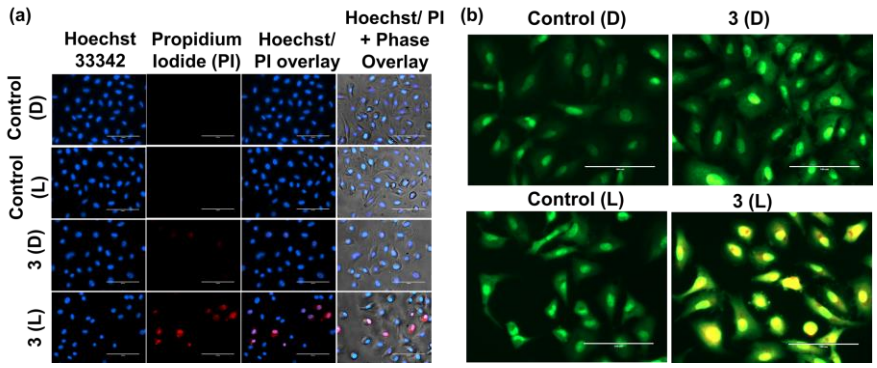


**Figure 2.18:** (a) Apoptotic cell death induced by **3** (at light $IC_{50}$ concentration) was evaluated through Hoechst 33342 and propidium iodide (PI) co-staining (L = light; D = dark). Incubation time with **3**: 6 h, Light irradiation (400-700 nm, 10 J $cm^{-2}$) for 2 min. Recovery after irradiation: 18 h. For the dark group, the light irradiation step was absent. Scale bar = 100 μm. The experiment was repeated three times independently with similar results. (b) AO and EB dual staining images of A549 cells collected from the control (dark and light) and **3** (at light $IC_{50}$ concentration) under dark and light irradiation (400-700 nm, 10 J $cm^{-2}$) groups (L = light; D = dark). Incubation time with **3**: 6 h, Light irradiation (400-700 nm, 10 J $cm^{-2}$) for 2 min. Recovery after irradiation: 18 h. For the dark group, the light irradiation step was absent. Scale bar: 100 μm. The experiment was repeated three times independently with similar results.

further confirming that **3** induced apoptosis upon photoactivation. To confirm these findings, we conducted an acridine orange/ethidium bromide (AO/EB) dual staining assay (Figure 2.18b). AO intercalates with DNA and emits green fluorescence in viable cells, while EB stains fragmented DNA and apoptotic nuclei, producing orange/red fluorescence.[48,49] The study revealed that, in the control group, A549 cells exhibited intact nuclear and cytoplasmic morphology with uniform green fluorescence under both dark and light irradiation (Figure 2.18b). However, upon treatment with **3** (at its light $IC_{50}$ concentration)+Light, cells displayed orange/red fluorescence with condensed chromatin, indicating late apoptotic cells, while yellowish-green fluorescence suggested early apoptotic cells at $IC_{50}$ concentrations (Figure 2.18b). These findings further confirmed that **3** induced apoptosis as the primary mode of cell death.

To quantitatively assess the cell death pathways, we performed Annexin V/PI assays with flow cytometry.[50] Annexin V/PI staining (followed by flow cytometry) is one of the prominent methods to quantitatively distinguish apoptosis or necrosis.[50] During apoptosis, the phosphatidylserine relocates to the outer layer of the cell membrane and binds with Annexin V.[50] Whereas, PI can enter only in cells with compromised membranes and bind to DNA, indicating necrosis or late apoptosis.[50] The study revealed that when A549 cells were treated with **3** (at light $IC_{50}$ concentration) in the absence of light, only about 15% of the cells were apoptotic (Figure 2.19). However, upon light exposure, the percentage of apoptotic cells increased significantly to 80% (early + late apoptotic cells) (Figure 2.19). These results strongly indicated that light-activated **3** (at its light $IC_{50}$ concentration) effectively induces apoptosis as the primary mode of cell death. Previous studies have also

demonstrated that Ir(III)-based cyclometalated polypyridyl photocatalysts induce cell death through apoptosis.[6,7]

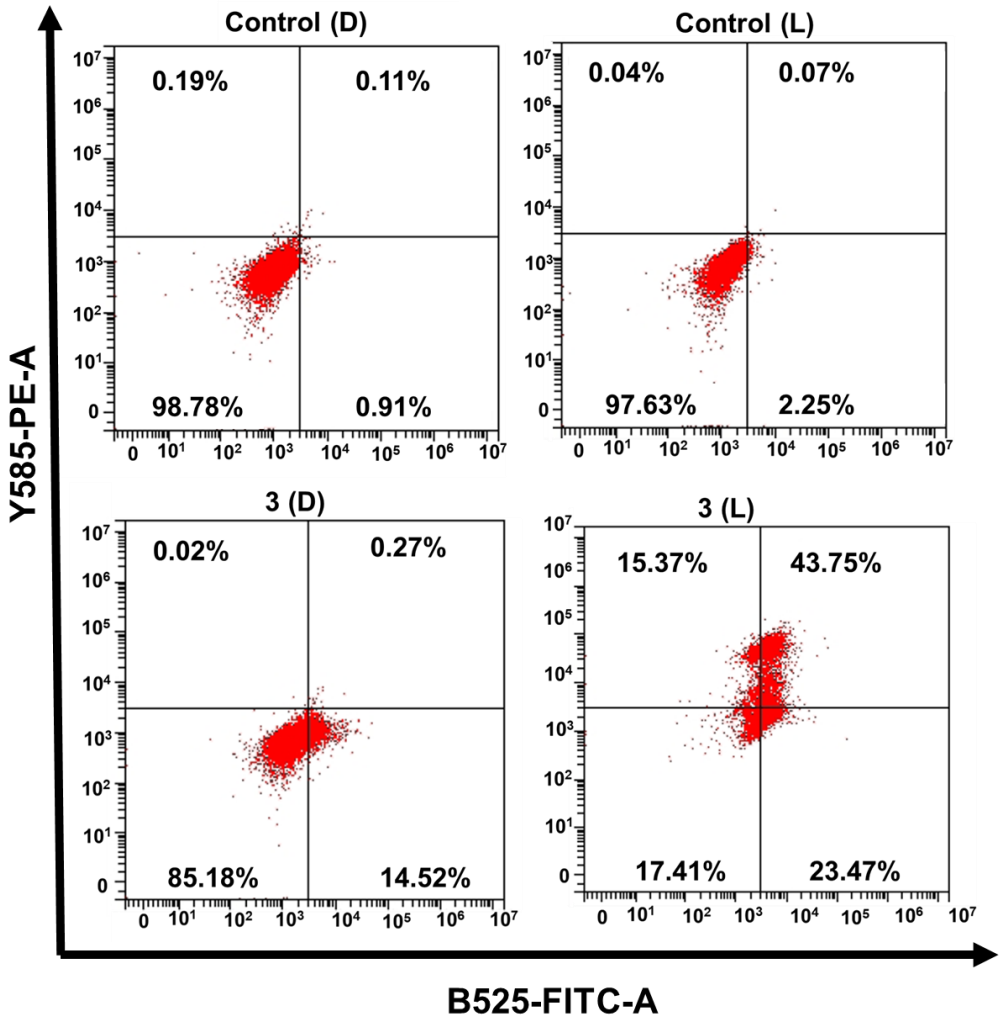


**Figure 2.19:** Quantitative determination of cell death by **3** (at its light $IC_{50}$ concentration) using flow cytometry using AnnexinV/PI assay (L = light; D = dark). Incubation time with **3**: 6 h, Light irradiation (400-700 nm, 10 J $cm^{-2}$) for 2 min. Recovery after irradiation: 18 h. For the dark group, the light irradiation step was absent. The experiment was repeated three times independently with similar results.

### 2.3.9. Caspase 3/7 activation

A defining feature of apoptosis is the sequential activation of caspase-3 and caspase-7, which serve as the executioner caspases in the apoptotic pathway.[51,52] Their activation cleaves key cellular proteins, ultimately resulting in programmed cell death.[51,52] To assess the involvement of caspases, we analyzed caspase-3/7 activation in A549 cells treated with **3** (at its light $IC_{50}$ concentration) under dark and light conditions using a caspase-3/7 green detection reagent in combination with SYTOX staining.[51,52] As illustrated in Figure 2.20a, A549 cells exposed to **3** (at its light $IC_{50}$ concentration) under dark conditions showed negligible activation of caspase-3/7, indicating limited initiation of apoptosis. In contrast, light irradiation significantly elevated caspase-3/7

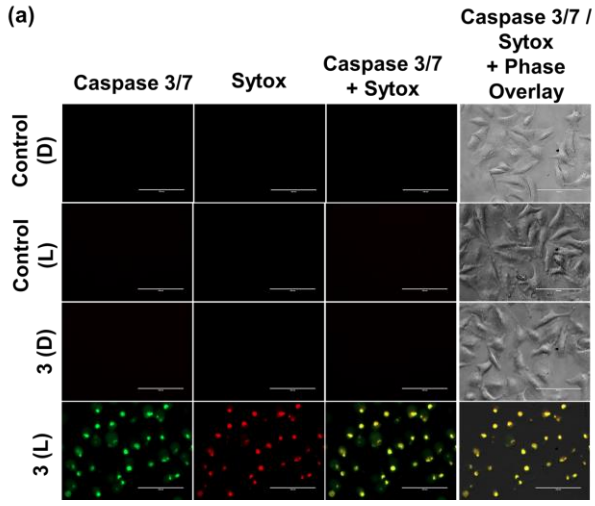


**Figure 2.20:** (a) The activation of caspase 3/7 was detected with cell event caspase-3/7 green detection reagent and SYTOX red in the presence of **3** (at its light $IC_{50}$ concentration)+Light (400-700 nm, 10 J $cm^{-2}$) (L = light; D = dark). Incubation time with **3**: 12 h, Light irradiation (400-700 nm, 10 J $cm^{-2}$) for 2 min. Recovery after irradiation: 12 h. For the dark group, the light irradiation step was absent. Scale bar = 100 μm. The experiment was repeated three times independently with similar results.

activity compared to the dark-treated group. These results suggest that **3** (at its light $IC_{50}$ concentration)+Light effectively promotes the activation of the executioner caspases-caspase-3/7, thereby facilitating apoptotic cell death. Flow cytometry data also suggested ~40% of caspase 3/7 activation in the presence of **3** (at its light $IC_{50}$ concentration)+Light (Figure 2.20b). As **3** promotes intracellular ROS generation and facilitates NADH oxidation upon light activation, thus the resulting oxidative stress and redox imbalance likely impair the electron transport chain and disrupt cellular energy homeostasis. This cascade of events leads to a loss of MMP, triggering

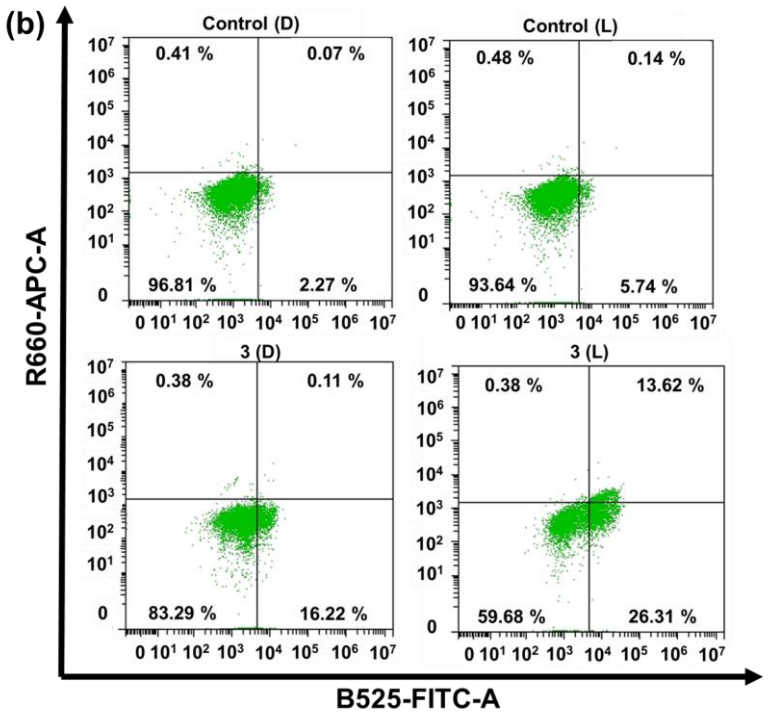


**Figure 2.20:** (b) Quantitative determination of the caspase 3/7 activation by **3** (at light $IC_{50}$ concentration) using flow cytometry (L = light; D = dark). Incubation time with **3**: 12 h, Light irradiation (400-700 nm, 10 J $cm^{-2}$) for 2 min. Recovery after irradiation: 12 h. For the dark group, the light irradiation step was absent. The experiment was repeated three times independently with similar results.

mitochondrial depolarization and activation of caspase-3/7, thereby initiating apoptotic cell death in cancer cells.

### 2.4. Conclusions

This Chapter successfully highlights the potential of novel Ir(III)-based photocatalysts (**1**-**3**) for cancer treatment. The photocatalysts (**1**-**3**) were synthesized in good yield, and various characterization techniques confirmed the structural integrity and purity of **1**-**3**. Their photophysical properties, including absorption in the visible region and in-solution $^1O_2$ generation quantum yields (0.14 - 0.18), supported their applicability in light-activated cancer therapies. Their ability to induce oxidative stress, mitochondrial dysfunction, and caspase-3/7 activation under light irradiation underscored their role in promoting apoptosis in cancer cells. Notably, their NADH oxidation capability further enhanced their anticancer efficacy by disrupting metabolic pathways.[1-8] Furthermore, **3** displayed high TOF (*ca.* 697.4 $h^{-1}$) compared to previously reported Ir(III) based photocatalysts,[1,8,9] indicating their efficiency in catalytic NADH oxidation and $H_2O_2$ generation. Cytotoxicity assays revealed that **1**-**3** exhibited potent photocytotoxicity with $IC_{50}$ values of ~ 0.8-2.3 μM, while maintaining minimal toxicity towards normal cells. The high selectivity for cancer cells over normal cells, combined with efficient photophysical properties and high catalytic performance, established these Ir(III)-based photocatalysts as promising candidates for developing targeted light-activated anticancer strategies. The structure-activity correlation derived from the present study is also expected to be useful for the design and development of next-generation Ir(III)-based photocatalysts with further improved selectivity towards cancer cells by varying coordinating moieties/groups.

## 2.5. Experimental section

### 2.5.1. Materials

$IrCl_3.xH_2O$, $[Ru(bpy)_3]Cl_2$, and 2-(4-(Triflurомethyl) phenyl) pyridine were purchased from Merck India Pvt. Ltd. 1,10 phenanthroline, ammonium acetate, ammonia solution, ethyl acetate, methanol, and ammonium hydroxide were purchased from BLD pharma (India). Formaldehyde, phenyl carboxaldehyde, and anthracene carboxaldehyde were purchased from Finar Ltd. (India). 1,3-diphenylisobenzofuran (DPBF), 2′,7′-Dichlorodihydrofluorescein diacetate (DCFDA), β-Nicotinamide adenine dinucleotide reduced disodium salt (β-NADH), Quantofix peroxide test sticks, dulbecco′s phosphate buffered saline were purchased from Sigma Aldrich. Hexane, dimethyl sulfoxide (DMSO), were purchased from Merck Life Science Pvt. Ltd. A549, and HEK-293 cell lines were procured from NCCS Pune India. DMEM and 12 well cell culture plates were purchased from Genetix Pvt. Ltd. T-25 flask, and 96 well plates were obtained from Eppendorf. MTT (3-(4,5- Dimethylthiazol-2-yl)-2,5-Diphenyltetrazolium Bromide) was obtained from SRL. FBS (Fetal Bovine Serum), Trypsin-EDTA, and Penicillin-streptomycin were procured from Gibco. JC-1 dye was procured from Cayman USA. Hoechst 33342 and PI (propidium iodide) were purchased from Lobachemie. The cell event caspase 3/7 activity assay kit was procured from Invitrogen, USA, through local vendors. PBS, pH = 7.0 was prepared in the laboratory. All the imidazo-phenanthroline-based ligands (ip, Ph-ip, and aip) were synthesized according to known literature procedures with some modifications.[53]

### 2.5.2. Instruments

UV-Vis. spectra of **1**-**3** were recorded using an Agilent Cary 60 UV-vis spectrophotometer. Fluorescence measurements were performed on a Techcomp FL970 fluorescence spectrophotometer. Electrospray ionization mass spectrometry (ESI-MS) of photocatalysts **1** and **2** were recorded using a Bruker micrOTOF-Q II, and the HRMS spectrum of photocatalyst **3** was recorded using a Bruker maXis Impact mass spectrometer. To record NMR spectra, an AVH D 500 AVANCE III HD 500 MHz OneBay NMR Spectrometer was used. EVOS FL Fluorescence microscopy from Life Technologies was used for cell imaging. Beckman Coulter CytoFLEX LX was used for the FACS analysis.

### 2.5.3. General synthetic procedure

The ligands (ip, ph-ip, and aip) were synthesized by previously established protocol.[53] A reflux reaction was carried out for 30 hours using 1,10-phenanthroline-5,6-dione and three different aldehydes (formaldehyde, phenyl carboxaldehyde, and anthracene carboxaldehyde) in a 1:1 molar ratio in the presence of an excess of ammonium acetate, with the reactants dissolved in a minimal volume of glacial acetic acid. The reaction progress was monitored using TLC to confirm the formation of the desired ligands (ip, ph-ip, and aip). The product was precipitated upon neutralization with ice-cold ammonium hydroxide solution, followed by filtration to obtain the crude product. The crude product was then thoroughly washed with hexane and diethyl ether to remove impurities and purified using recrystallization to obtain pure crystalline ligands.

### 2.5.4. Synthetic procedure of $[Ir(C^N)_2Cl]_2$

A mixture of 2 equiv. of 2-(4-(Trifluromethyl) phenyl) pyridine and 1 equiv. of $IrCl_3 \cdot xH_2O$ in a binary solvent system (2-ethoxyethanol (6 mL) and water (2 mL)) was heated at 120 °C for 24 h (Scheme 2.1). Thereafter, an orange colour precipitate was obtained. The precipitate was filtered, washed with water, and dried to get the desired product.

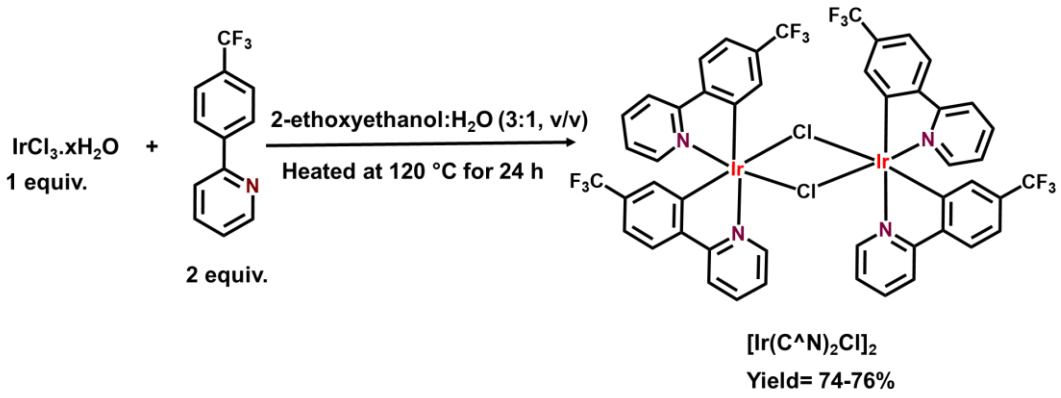


**Scheme 2.1:** General synthetic pathway for $[Ir(C^N)_2Cl]_2$.

### 2.5.5. General synthetic procedure for Photocatalysts (1-3)

1 equiv. of $[Ir(C^N)_2Cl]_2$, and 2.1 equiv. of corresponding N^N donor ligand were placed in an oven-dried round-bottom flask, and then $CHCl_3$/MeOH (18 mL; 2:1 v/v) was introduced. The resulting mixture was heated at 50 °C for 24 h (Scheme 2.2). Thereafter, the solution was cooled at ambient temperature, and the solvent was removed on a rotary evaporator. The deep yellow to reddish-brown solid was washed with diethyl ether. The crude product was purified by column chromatography on neutral alumina, eluted with methanol and n-hexane (1:99, v/v). The product was dried under a vacuum to yield a deep yellow to brown powder.

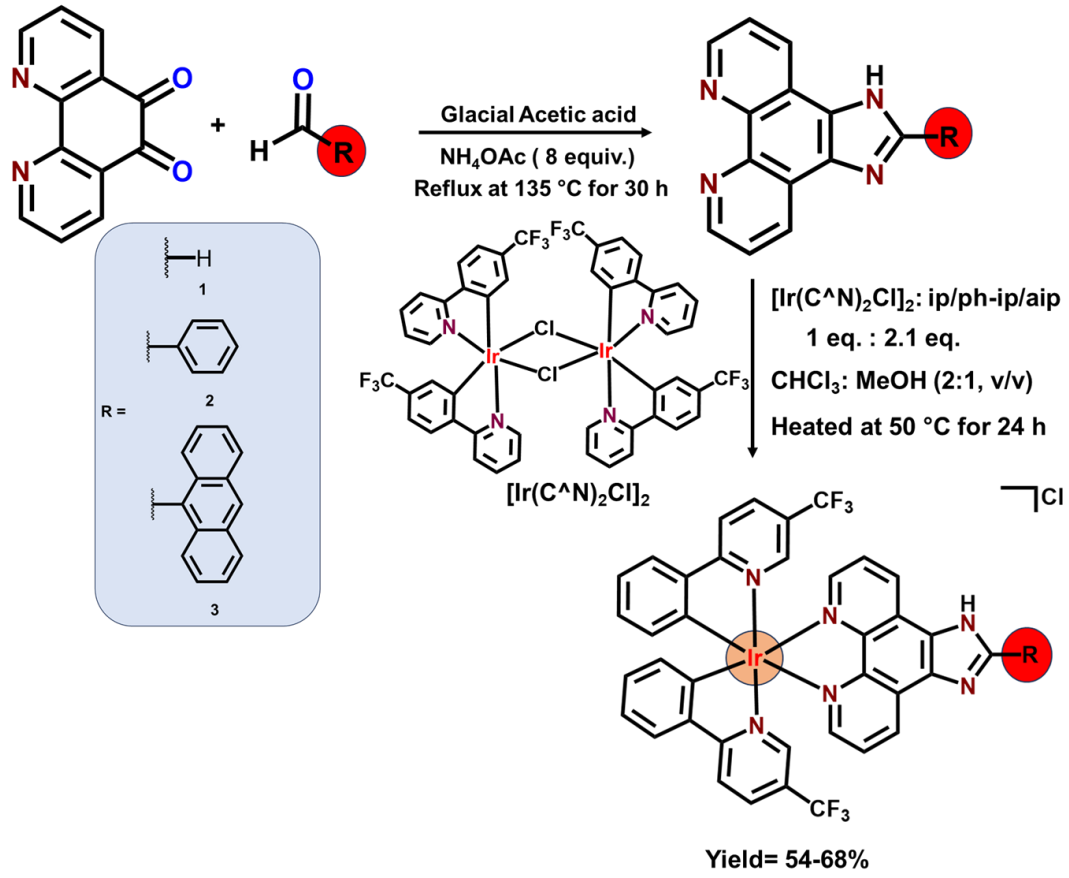


**Scheme 2.2:** General synthetic pathway for the synthesis of **1-3**.

Photocatalyst **1**: Yield = 68 %, $C_{37}H_{22}ClF_6IrN_6$ (MW = 892.28 g/mol). Elemental analysis: calcd: C = 49.81, H = 2.49, N = 9.42, obtained: C = 49.57, H = 2.72, N = 9.26. UV-Vis. spectral data were recorded in DMSO:PBS (1:99, v/v) where $\lambda_{max}$ = 383 nm ($\varepsilon = 1.84 \times 10^3$ $M^{-1}$ $cm^{-1}$), and $\lambda_{max}$ = 416 nm ($\varepsilon = 1.03 \times 10^3$ $M^{-1}$ $cm^{-1}$). Emission spectra were recorded in DMSO:PBS (1:99, v/v) $\lambda_{ex}$ = 380 nm, $\lambda_{em}$ = 527 nm. ESI-MS (m/z for $[M]^+$) in MeOH: expected = 857.1439, obtained = 857.1639. $^1$H NMR (500 MHz, DMSO-$d_6$, ppm) δ: 9.21 (d, *J* = 7.8 Hz, 2H), 8.47 (d, *J* = 8.1 Hz, 2H), 8.40 (d, *J* = 7.5 Hz, 2H), 8.21 (d, *J* = 8.1 Hz, 2H), 8.01 (dd, *J* = 6.5 Hz, 4H), 7.97 – 7.92 (m, 2H), 7.64 (d, *J* = 5.3 Hz, 2H), 7.49 (t, *J* = 7.3 Hz, 2H), 7.40 (d, *J* = 7.8 Hz, 3H), 7.17 (dd, *J* = 7.4 Hz, 2H), 6.46 (s, 2H). $^{13}$C NMR

(125 MHz, DMSO-$d_6$, ppm) δ: 165.47, 162.52, 148.88, 144.35, 140.00, 130.17, 127.69, 126.84, 125.94, 125.29, 123.28, 121.92, 120.07.

Photocatalyst **2**: Yield = 63 %, $C_{43}H_{26}ClF_6IrN_6$ (MW = 968.38 g/mol). Elemental analysis: calcd: C = 53.33, H = 2.71, N = 8.68, obtained: C = 53.51, H = 2.47, N = 8.39. UV-Vis. spectral data were recorded in DMSO:PBS (1:99, v/v) where $\lambda_{max}$ = 390 nm (ε = 2.80 × $10^3$ $M^{-1}$ $cm^{-1}$), and $\lambda_{max}$ = 418 nm (ε = 1.99 × $10^3$ $M^{-1}$ $cm^{-1}$). Emission spectra were recorded in DMSO:PBS (1:99, v/v) $\lambda_{ex}$ = 380 nm, $\lambda_{em}$ = 530 nm. ESI-MS (m/z for $[M]^+$) in MeOH: expected = 933.1752, obtained = 933.1930. $^1$H NMR (500 MHz, DMSO-$d_6$, ppm) δ: 9.15 (d, *J* = 5.1 Hz, 1H), 8.46 (d, *J* = 8.0 Hz, 3H), 8.21 (d, *J* = 7.8 Hz, 3H), 8.01 (d, *J* = 6.3 Hz, 4H), 8.00 (d, 2H), 7.62 (d, *J* = 4.4 Hz, 2H), 7.40 (d, *J* = 7.7 Hz, 2H), 7.15 (d, 2H), 6.46 (s, 2H). $^{13}$C NMR (125 MHz, DMSO-$d_6$, ppm) δ: 165.69, 151.61, 149.93, 148.80, 146.33, 142.87, 139.85, 132.39, 128.79, 126.87, 126.28, 125.89, 121.73, 119.79.

Photocatalyst **3**: Yield = 54 %, $C_{51}H_{30}ClF_6IrN_6$ (MW = 1068.50 g/mol). Elemental analysis: calcd: C = 57.33, H = 2.83, N = 7.87, obtained: C = 57.51, H = 2.57, N = 7.58. UV-Vis. spectral data were recorded in DMSO: PBS (1:99, v/v) where $\lambda_{max}$ = 390 nm (ε = 3.73 × $10^3$ $M^{-1}$ $cm^{-1}$) and $\lambda_{max}$ = 425 nm (ε = 1.84 × $10^3$ $M^{-1}$ $cm^{-1}$). Emission spectra were recorded in DMSO:PBS (1:99, v/v) $\lambda_{ex}$ = 380 nm, $\lambda_{em}$ = 442 and 475 nm. HR-MS (m/z for $[M]^+$) in MeOH: expected = 1033.2065, obtained = 1033.2028. $^1$H NMR (500 MHz, DMSO-$d_6$, ppm) δ: 8.99 (s, 1H), 8.51 (d, *J* = 8.2 Hz, 2H), 8.31 (d, *J* = 8.5 Hz, 2H), 8.25 (d, *J* = 8.2 Hz, 3H), 8.20 (d, *J* = 5.0 Hz, 2H), 8.13 (dd, *J* = 5.3 Hz, 2H), 8.08 (t, *J* = 7.8 Hz, 2H), 7.81 (d, *J* = 8.7 Hz, 2H), 7.75 (d, *J* = 5.7 Hz, 2H), 7.65 (t, *J* = 7.5 Hz, 3H), 7.62 – 7.54 (m, 2H), 7.46 (d, *J* = 8.2 Hz, 2H), 7.22 (t, *J* = 6.7 Hz, 2H), 6.48 (s, 2H). $^{13}$C NMR (125 MHz, DMSO-$d_6$,

ppm) δ: 194.53, 139.90, 135.72, 135.03, 131.83, 131.41, 131.14, 129.81, 129.75, 129.20, 127.23, 126.31, 126.27, 125.48, 124.90, 123.95, 103.65.

### 2.5.6. NMR spectrometer

$^{1}H$ and $^{13}C$ nuclear magnetic resonance (NMR) spectra were obtained at magnetic field strengths of 500 MHz and 125 MHz respectively. DMSO-$d_6$ solutions were used to record spectra. MestReNova software was used for data processing.

### 2.5.7. UV-visible spectroscopy

UV-Visible (UV-Vis.) absorption spectra of **1**-**3** were acquired in DMSO:PBS (1:99, v/v) solvent mixture using 1 cm path-length quartz cuvettes with an Agilent Cary 60 UV-Vis. spectrophotometer. The measurements were performed across a wavelength range of 200-800 nm. The software Origin Pro 2019 was then used to process the acquired data.

### 2.5.8. Fluorescence spectra

The fluorescence spectra of **1**-**3** (50 μM) in DMSO:PBS (1:99, v/v) solution were recorded with an excitation at $\lambda_{ex}$ = 380 nm in a 1 cm quartz cuvette.

### 2.5.9. Photo-stability study

UV-Vis. spectral measurement in a time-dependent fashion was used to conduct the photo-stability study.[5-8] The experiment was conducted at ambient temperature in DMSO:PBS (1:99, v/v) solution. For the photostability experiment, the solution of **1**-**3** (20 μM) was kept under visible light (400-700 nm, 10 J $cm^{-2}$), and UV-Vis. absorption spectra were recorded from 0-7 h.

### 2.5.10. Photocatalytic reactions of 1-3 with NADH

Reactions between **1-3** (1 μM each), and NADH (175 μM) in DMSO:PBS (1:99, v/v) solution at different time intervals were monitored by UV-Vis. spectroscopy on irradiation with visible light (400-700 nm).[1-8] Turnover number (TON) is defined as the number of moles of NADH that a mole of the catalyst can convert within 10 min. Turnover frequency (TOF) was calculated from the difference in NADH concentration after 10 min irradiation divided by the concentration of respective catalysts.

$[NAD^+] = [Abs(339\ nm)_{initial} - Abs(339\ nm)_{final}]/Abs(339\ nm)_{initial} \times [NADH]$

Turnover number (TON) = $[NAD^+]$/[Catalyst]

Turnover frequency (TOF) = Turnover number/Time (h).

### 2.5.11. Detection of $H_2O_2$ generation

In the reaction of **3** (1 μM) with NADH (175 μM) in DMSO:PBS (1:99, v/v) at ambient temperature under both dark and light irradiation (400-700 nm, 10 J $cm^{-2}$), $H_2O_2$ was detected by Quantofix peroxide test sticks.[5-7]

### 2.5.12. Detection of singlet oxygen ($^1O_2$) generation

The production of photo-induced $^1O_2$ by **1-3** was detected using the singlet oxygen sensor DPBF.[23,24] Briefly, **1-3** (1 μM each) in DMSO:PBS (1:99, v/v) was mixed with DPBF (50 μM). The solution was then placed in quartz cuvettes, followed by 400-700 nm (10 J $cm^{-2}$) light irradiation for different time intervals. The absorbance of the DPBF was then monitored by UV-Vis. spectroscopy. The $^1O_2$ generation quantum yield ($\Phi_\Delta$) of **1-3** was

measured by recording UV-Vis. absorption spectra of DPBF from 200-800 nm. The relative $^1O_2$ generation quantum yields were determined with $[Ru(bpy)_3]Cl_2$ ($\Phi_{\Delta s}$ = 0.22 in aq. DMSO)[29] as the standard using the following equation: $\Phi_{\Delta x} = \Phi_{\Delta s} \times (F_x/F_s) \times (A_s/A_x)$ Where $\Phi_\Delta$ represents $^1O_2$ generation quantum yield; F stands for the integrated area under the corrected absorption spectrum; A is the absorbance at 419 nm. The subscripts x and s refer to the photocatalyst sample and the standard, respectively.

**2.5.13. MTT assay**

The cytotoxicity assay of **1-3** has been performed against A549 (lung adenocarcinoma), and HEK-293 cells (human embryonic kidney cells). 10,000 cells/well were seeded in 2 different (one for light exposure, the second for dark conditions) 96-well plates in DMEM with 10% FBS and 1% penicillin-streptomycin solution, and placed in a 37 ℃, 5% $CO_2$ incubator for 24 h to equilibrate and allow cell attachment. After that, the medium was removed completely, and the fresh medium containing different concentrations of **1-3** (0.5 μM, 1 μM, 5 μM, 10 μM, and 25 μM) was added to each well, and kept for a 6 h incubation in a 5% humidified $CO_2$ incubator at 37˚C. The percentage of DMSO in the culture media was within the permissible limit (<1%). Thereafter, the drug-containing medium was discarded, and 100 μL PBS (phosphate buffer saline) was added to each well of all treated 96-well plates. One of those plates was exposed to light (Light source: 400-700 nm, 10 J $cm^{-2}$), and subsequently, one was kept in a dark condition. After light irradiation, PBS was removed from both plates, and a fresh DMEM medium was added to each and incubated for another 18 h at 37 °C in a humidified 5% $CO_2$ incubator. Finally, the medium was discarded, and the fresh MTT-containing medium was added to each well. After 2 h of

incubation, the MTT-containing medium was removed, and the formazan product was dissolved in 100 µL of DMSO and further incubated for 0.5 h. The cell viability was evaluated by measurement of the absorbance at 570 nm, using a multiplate reader. $IC_{50}$ values were calculated from curves constructed by plotting cell survival (%) versus drug concentration (µM). All experiments were made in triplicate.

### 2.5.14. DCFHDA assay

To study the intracellular ROS generation by **3** inside the A549 cells, we performed the DCFHDA assay.[33,34] In brief, the assay was performed by seeding $0.5 \times 10^5$ A549 cells/well in two 12-well cell culture plates (one for light exposure, the second one for dark conditions) in DMEM with 10% FBS and 1% penicillin-streptomycin solution, and incubated 24 h for adherence. The cells were then treated with **3** at its light $IC_{50}$ value concentration and kept for a 6 h incubation in a 5% humidified $CO_2$ incubator at 37 °C. Thereafter, the drug-containing medium was discarded, and 100 µL PBS was added to each well of all treated 12-well plates. One of those plates was exposed to light (Light source: 400-700 nm, 10 J $cm^{-2}$, 2 min), and subsequently, one was kept in a dark condition. After light irradiation, PBS was removed from both plates, and a fresh DMEM medium was added and incubated for another 18 h in a 5% humidified $CO_2$ incubator at 37 °C. The cells were washed with PBS, then treated with 10 µM DCFH-DA and incubated at 37 °C for 30 minutes in a humidified incubator containing 5% $CO_2$. Finally, images were photographed in a fluorescent microscope set to excitation at 450-490 nm and emission at 500-550 nm filters under green channels and phase contrast at 400X magnification.

### 2.5.15. JC-1 assay

To study the change in mitochondrial membrane potential, we performed JC-1 assay.[42,43] The assay was performed by seeding approximately 0.5 × $10^5$ A549 cells/well in two 12-well cell culture plates (one for light exposure, the second one for dark conditions) supplemented with DMEM with 10% FBS and 1% penicillin-streptomycin solution, and incubated for 24 h for adherence. The cells were then treated with **3** at its light $IC_{50}$ value concentration and kept for a 6 h incubation in a 5% humidified $CO_2$ incubator at 37 °C. Thereafter, the drug-containing medium was discarded, and 100 µL PBS was added to each well of all treated 12-well plates. One of those plates was exposed to light (Light source: 400-700 nm, 10 J $cm^{-2}$, 2 min), and subsequently, one was kept in a dark condition. After light irradiation, PBS was removed from both plates, and a fresh DMEM medium was added and incubated for another 18 h in a 5% humidified $CO_2$ incubator at 37 °C. The cells were washed with PBS, then stained with 1 µM JC-1 dye and incubated at 37 °C for 30 minutes in a humidified incubator containing 5% $CO_2$. Fluorescence-emitting images were captured at 100X magnification (EVOS FL by Life Technology). For capturing images, excitation was done primarily at 488 nm, while emissions were detected at both 530 nm (green for monomers) and 595 nm (orange-red for aggregates).

### 2.5.16. Apoptosis study by Hoechst 33342/PI dual staining

To investigate the nuclear morphology changes after treatment of **3**, we performed Hoechst 33342/PI dual staining.[44,45] In brief, the assay was performed by seeding 0.5 × $10^5$ A549 cells/well in two 12-well cell culture plates (one for light exposure, the second one for dark conditions) supplemented with DMEM with 10% FBS and 1% penicillin-streptomycin

solution, and incubated for 24 h for adherence. The cells were then treated with **3** at its light $IC_{50}$ value concentration and kept for a 6 h incubation in a 5% humidified $CO_2$ incubator at 37 °C. Thereafter, the drug-containing medium was discarded, and 100 µL PBS was added to each well of all treated 12-well plates. One of those plates was exposed to light (Light source: 400-700 nm, 10 J $cm^{-2}$, 2 min), and subsequently, one was kept in a dark condition. After light irradiation, PBS was removed from both plates, and a fresh DMEM medium was added and incubated for another 18 h in a 5% humidified $CO_2$ incubator at 37 °C. The cells were washed with PBS, then stained with 10 µg/mL PI and 10 µg/mL Hoechst 33342 and incubated at 37 °C for 30 minutes in a humidified incubator containing 5% $CO_2$ and then images were captured in a fluorescent microscope in phase contrast, red and blue channels at 100X magnification. The images were captured at 350 nm excitation/454-497 nm emission for Hoechst 33342, and 488 nm excitation/615-635 nm emission for PI.

### 2.5.17. AO/EB dual staining

To assess cellular morphology changes during apoptosis following treatment of **3**, we performed AO/EB dual staining assay.[48] The assay was performed by seeding $0.5 \times 10^5$ A549 cells/well in two 12-well cell culture plates (one for light exposure, the second one for dark conditions) supplemented with DMEM with 10% FBS and 1% penicillin-streptomycin solution, and incubated for 24 h for adherence. The cells were then treated with **3** at its light $IC_{50}$ value concentration and kept for a 6 h incubation in a 5% humidified $CO_2$ incubator at 37˚C. Thereafter, the drug-containing medium was discarded, and 100 µL PBS was added to each well of all treated 12-well plates. One of those plates was exposed to light (Light source: 400-700 nm, 10 J $cm^{-2}$, 2 min), and subsequently, one was kept in a

dark condition. After light irradiation, PBS was removed from both plates, and a fresh DMEM medium was added and incubated for another 18 h in a 5% humidified $CO_2$ incubator at 37 °C. The cells were washed with PBS, then stained with AO/EB (20 µg/mL each) and incubated at 37 °C for 30 minutes in a humidified incubator containing 5% $CO_2$, and images were captured using a fluorescence microscope (100X) under red and green channels. The images were recorded at 488 nm excitation/525 nm emission for AO, and 488 nm excitation/616-635 nm emission for EB.

### 2.5.18. Annexin V-FITC/PI staining

To quantify apoptotic cell populations following **3** treatment, Annexin V/PI assay was performed.[50] The assay was performed by seeding $1.0 \times 10^6$ A549 cells/well in two 6-well cell culture plates (one for light exposure, the second one for dark conditions) supplemented with DMEM with 10% FBS and 1% penicillin-streptomycin solution, and incubated for 24 h for adherence. The cells were then treated with **3** at its light $IC_{50}$ value concentration and kept for a 6 h incubation in a 5% humidified $CO_2$ incubator at 37˚C. Thereafter, the drug-containing medium was discarded, and 100 µL PBS was added to each well of all treated 6-well plates. One of those plates was exposed to light (Light source: 400-700 nm, 10 J $cm^{-2}$, 2 min), and subsequently, one was kept in a dark condition. After light irradiation, PBS was removed from both plates, and a fresh DMEM medium was added and incubated for another 18 h in a 5% humidified $CO_2$ incubator at 37 °C. Afterward, cells were harvested with help of ice chilled 1 mM EDTA in PBS (pH 7.4), and centrifuged at 3000 rpm for 5 minutes. Supernatant were discarded. Subsequently, staining was done based on the manufacturer's protocol for Alexa Fluor 488 Annexin V/PI staining (Thermo Fisher

Scientific, Invitrogen Bioservices India Pvt. Ltd.) The images were captured at 488 nm excitation/530 nm emission for Annexin V-FITC, and 488 nm excitation/615-630 nm emission for PI). The flow cytometer (Beckman coulter) was used to immediately analyze the apoptosis.

**2.5.19. Caspase 3/7 assay**

The assay was performed by seeding $0.5 \times 10^5$ A549 cells/well in two 12-well cell culture plates (one for light exposure, the second one for dark conditions) supplemented with DMEM with 10% FBS and 1% penicillin-streptomycin solution, and incubated for 24 h for adherence. The cells were then treated with **3** at its light $IC_{50}$ concentration and kept for a 12 h incubation in a 5% humidified $CO_2$ incubator at 37 °C. Thereafter, the drug-containing medium was discarded, and 100 µL PBS was added to each well of all treated 12-well plates. One of those plates was exposed to light (Light source: 400-700 nm, 10 J $cm^{-2}$, 2 min), and subsequently, one was kept in a dark condition. After light irradiation, PBS was removed from both plates, and a fresh DMEM medium was added and incubated for another 12 h in a 5% humidified $CO_2$ incubator at 37 °C. After 12 h incubation, cells were harvested with the help of ice chilled 1 mM EDTA in PBS (pH 7.4), and centrifuged at 3000 rpm for 5 minutes. Supernatant were discarded. Subsequently, the cells were stained with 1 µL of caspase3/7 and followed by the addition of 1 µL of SYTOX per sample and incubated at 37 °C for 30 minutes in a humidified incubator containing 5% $CO_2$. Finally, the images were captured in green, red, and phase contrast channels through an EVOS FL microscope at 100X magnification equipped with a 488-nm laser. The green fluorescence emission was collected using a 530 nm bandpass filter for CellEvent™ Caspase-3/7 Green

detection reagent, and a red fluorescence emission was collected at a 690 nm bandpass filter for SYTOX™ AADvanced™ Dead Cell Stain, respectively. For quantitative analysis, cells were seeded in two 6-well cell culture plates (one for light exposure, the second one for dark conditions) supplemented with DMEM with 10% FBS and 1% penicillin-streptomycin solution, incubated for 24 h for adherence. The cells were then treated with **3** at its light $IC_{50}$ concentration and kept for a 12 h incubation in a 5% humidified $CO_2$ incubator at 37 °C. After 12 h incubation, cells were harvested using 1 mM EDTA solution in ice-cold PBS and centrifuged at 3000 rpm for 5 minutes. The supernatant was subsequently removed, and the pellet was resuspended in PBS. The staining procedure was the same as the above-mentioned protocol. The flow cytometer (Beckman Coulter, USA) was used immediately to quantitatively analyze the caspase 3/7 activation.[54]

### 2.5.20. Statistical analysis

The results was expressed as mean ± standard error of the three independent repeated experiments. Sample size, i.e., n = 3, was used for respective statistical analysis. The statistical analysis was conducted utilizing SPSS 16.0 (SPSS, Chicago, IL, USA) software. Results were compared between the dark control with the rest of the group (**3**, Control light, and **3**+Light). The statistical analysis was done by One-way ANOVA followed by Tukey's Post Hoc Test. Values of $p<0.05$ were considered statistically significant.

## 2.6. References:

1. H. Huang, S. Banerjee, K. Qiu, P. Zhang, O. Blacque, T. Malcomson, M. J. Paterson, G. J. Clarkson, M. Staniforth, V. G. Stavros, G. Gasser, H. Chao, P. J. Sadler, *Nat. Chem*. **2019**, *11*, 1041-1048.

2. Z. Fan, J. Xie, T. Sadhukhan, C. Liang, C. Huang, W. Li, T. Li, P. Zhang, S. Banerjee, K. Raghavachari, H. Huang, *Chem. Eur. J*. **2022**, *28*, e202103346.
3. L. Wei, R. Kushwaha, A. Dao, Z. Fan, S. Banerjee, H. Huang, *Chem. Commun*. **2023**, *59*, 3083-3086.
4. Z. Zhu, L. Wei, Y. Lai, W. L. O. Carter, S. Banerjee, P. J. Sadler, H. Huang, *Dalton Trans*. **2022**, *51*, 10875-10879.
5. Z. Fan, Y. Rong, T. Sadhukhan, S. Liang, W. Li, Z. Yuan, Z. Zhu, S. Guo, S. Ji, J. Wang, R. Kushwaha, S. Banerjee, K. Raghavachri, H. Huang, *Angew. Chem. Int. Ed*. **2022**, *61*, e202202098.
6. C. Huang, C. Liang, T. Sadhukhan, S. Banerjee, Z. Fan, T. Li, Z. Zhu, P. Zhang, K. Raghavachari, H. Huang, *Angew. Chem. Int. Ed.* **2021**, *60*, 9474-9479.
7. U. Das, P. Paira, *Dalton Trans.* **2024**, *53,* 6459-6471.
8. J. Kasparkova, A. H. García, H. Kostrhunova, M. Goicuría, V. Novohradsky, D. Bautista, L. Markova, M. D. Santana, V. Brabec, J. Ruiz, *J. Med. Chem*. **2024**, *11*, 691-708.
9. S. Ghosh, P. Paira, *Eur. J. Inorg. Chem.* **2025**, *28,* e202400769.
10. Z. Fan, J. Xie, R. Kushwaha, S. Liang, W. Li, A. A. Mandal, L. Wei, S. Banerjee, H. Huang, *Chem. Asian J.* **2023**, *18*, e202300047.
11. Y. Yang, Y. Gao, J. Zhao, S. Gou, *Inorg. Chem. Front*. **2024**, *11*, 436-450.
12. A. Dao, H. Wu, S. Wei, H. Huang, *Phys. Chem. Chem. Phys*. **2023**, *25*, 20001-20008.

13. M. J. M. Plata, L. Marretta, L. Gaztelumendi, G. E. Pieslinger, R. R. Carballo, E. Rezabal, G. Barone, V. M. Martínez, A. Terenzi, L. Salassa, *Inorg. Chem.* **2024**, *63*, 16362-16373.

14. A. Shimizu, Y. Ishizaki, S. Horiuchi, T. Hirose, K. Matsuda, H. Sato, J. I. Yoshida, *J. Org. Chem*. **2021**, *86*, 770-781.

15. S. G. Valenzuela, I. T. Moya, A. Sánchez, B. Donoso, J. T. L. Navarrete, M. C. R. Delgado, P. Prieto, R. P. Ortiz, *Chem. Eur. J.* **2023**, *29*, e202301639.

16. K. Sudhakar, A. Mizrahi, M. Kosa, N. Fridman, B. Tumanskii, M. Saphier, Z. Gross, *Angew. Chem. Int. Ed.* **2017**, *56*, 9837-9841.

17. X. Zhan, P. Teplitzky, Y. D. Posner, M. Sundararajan, Z. Ullah, Q. C. Chen, L. J. W. Shimon, I. Saltsman, A. Mahammed, M. Kosa, M. H. Baik, D. G. Churchill, Z. Gross, *Inorg. Chem*. **2019**, *58*, 6184-6198.

18. K. Sudhakar, A. Mahammed, N. Fridman, Z. Gross, *Dalton Trans*. **2019**, *48*, 4798-4810.

19. M. Mariappan, B. G. Maiya, *Eur. J. Inorg. Chem*. **2005**, *2005*, 2164-2173.

20. Y. Sun, J. Liu, X. Zhang, Z. Cao, L. Bu, S. Cao, X. Liu, X. A. Yuan, Z. Liu, *Inorg. Chem*. **2024**, *63*, 14641-14655.

21. W. A. Velema, W. Szymanski, B. L. Feringa, *J. Am. Chem. Soc.* **2014**, *136*, 2178-2191.

22. Y. Xu, Y. Pang, L. Luo, A. Sharma, J. Yang, C. Li, S. Liu, J. Zhan, Y. Sun, *Angew. Chem. Int. Ed.* **2024**, *63*, e202319966.

23. L. Qiao, J. Liu, S. Kuang, X. Liao, J. Kou, L. Ji, H. Chao, *Dalton Trans*. **2021**, *50*, 14332-14341.

24. A. Bera, S. Gautam, S. Sahoo, A. K. Pal, P. Kondaiah, A. R. Chakravarty, *RSC. Med. Chem*. **2022**, *13*, 1526-1539.

25. S. J. Chadwick, D. Salah, P. M. Livesey, M. Brust, M. Volk, *J. Phys. Chem. C* **2016**, *120*, 10647-10657.

26. D. Song, S. Cho, Y. Han, Y. You, W. Nam, *Org. Lett.* **2013**, *15*, 3582-3585.

27. J. M. Aubry, C. Pierlot, J. Rigaudy, R. Schmidt, *Acc. Chem. Res.* **2003**, *36*, 668-675.

28. A. Marco, J. Kasparkova, D. Bautista, H. Kostrhunova, N. Cutillas, L. Markova, V. Novohradsky, J. Ruiz, V. Brabec, *J. Med. Chem*. **2024**, *67*, 21470-21485.

29. P. Zhang, H. Huang, S. Banerjee, G. J. Clarkson, C. Ge, C. Imberti, P. J. Sadler, *Angew. Chem. Int. Ed.* **2019**, *58*, 2350-2354.

30. J. V. Meerloo, G. J. Kaspers, J. Cloos, *Methods Mol. Biol*. **2011**, *731*, 237-245.

31. N. P. Bigham, J. J. Wilson, *Eur. J. Inorg. Chem*. **2023**, *26*, e202200735.

32. S. Abdolmaleki, S. Khaskar, A. Aliabadi, A. Panjehpour, E. Motieiy, D. Marabello, M. H. Faraji, M. Beihaghi, *Toxicology* **2023**, *492*, 153516.

33. Y. Zhao, X. Ye, Z. Xiong, A. Ihsan, I. Ares, M. Martínez, B. L. Torres B, M. R. M. Larrañaga, A. Anadón, X. Wang, M. A. Martínez, *Metabolites* **2023**, *13*, 796.

34. S. Nikolić, J. Arakelyan, V. Kushnarev, S. M. Alfadul, D. Stanković, Y. I. Kraynik, S. G. Šipka, M. V. Babak, *Inorg. Chem*. **2023**, *62*, 8188-8199.

35. A. C. Carrasco, V. R. Fanjul, A. Habtemariam, A. M. Pizarro, *J. Med. Chem*. **2020**, *63*, 4005-4021.

36. E. Eruslanov, S. Kusmartsev, *Methods Mol. Biol*. **2010**, *594*, 57-72.

37. M. J. Reiniers, R. F. V. Golen, S. Bonnet, M. Broekgaarden, T. M. V. Gulik, M. R. Egmond, M. Heger, *Anal. Chem*. **2017**, *89*, 3853-3857.

38. A. Upadhyay, A. Nepalia, A. Bera, D. K. Saini, A. R. Chakravarty, *Chem. Asian J.* **2023**, *18*, e202300667.

39. R. J. Mitchell, A. S. Gowda, A. G. Olivelli, A. J. Huckaba, S. Parkin, J. M. Unrine, V. Oza, J. S. Blackburn, F. Ladipo, D. K. Heidary, E. C. Glazer, *Inorg. Chem*. **2023**, *62*, 10940-10954.

40. A. Poltorak, *Curr. Biol*. **2022**, *32*, R874-R896.

41. Y. Zong, H. Li, P. Liao, L. Chen, Y. Pan, Y. Zheng, C. Zhang, D. Liu, M. Zheng, J. Gao, *Sig. Transduct. Target Ther.* **2024**, *9*, 124.

42. D. G. Nicholls, M. W. Ward, *Trends Neurosci*. **2000**, *23*, 166-174.

43. M. Reers, T. W. Smith, L. B. Chen, *Biochemistry* **1991**, *18*, 4480-4486.

44. S. P. Vaidya, M. Patra, *Curr. Opin. Chem. Biol*. **2023**, *72*, 102236.

45. G. Sharma, N. K. Rana, P. Singh, P. Dubey, D. S. Pandey, B. Koch, *Biomed. Pharmacother*. **2017**, *88*, 218-231.

46. B. T. Grimberg, *J. Immunol. Methods* **2011**, *367*, 1-16.

47. S. Mukhopadhyay, R. K. Gupta, R. P. Paitandi, N. K. Rana, G. Sharma, B. Koch, L. K. Rana, M. S. Hundal, D. S. Pandey, *Organometallics* **2015**, *34*, 4491-4506.

48. A. Paul, P. Singh, M. L. Kuznetsov, A. Karmakar, M. F. C. G. D. Silva, B. Koch, A. J. L. Pombeiro, *Dalton Trans*. **2021**, *50*, 3701-3716.

49. G. B. Jiang, Y. Y. Xie, G. J. Lin, H. L. Huang, Z. H. Liang, Y. J. Liu, *J. Photochem. Photobiol. B*. **2013**, *129*, 48-56.

50. I. Vermes, C. Haanen, H. S. Nakken, C. Reutelingsperger, *J. Immunol. Methods*, **1995**, *184*, 39-51.

51. P. Goswami, V. Singh, B. Koch, *J. Ethnopharmacol*. **2024**, *334*, 118537.

52. H. R. Stennicke, J. M. Jurgensmeier, H. Shin, Q. Deveraux, B. B. Wolf, X. Yang, Q. Zhou, H. M. Ellerby, L. M. Ellerby, D. Bredesen, *J. Biol. Chem*. **1998**, *273*, 27084-27090.

53. B. N. Bideh, M. Moghadam, A. Sousaraei, B. S. Arani, *Sci. Rep.* **2023**, *13*, 2287.

54. S. Singh, V. Singh, R. Singh, V. Gouri, B. Koch, M. Samant, *Eur. J. Pharmacol*. **2025**, *992*, 177361.